REPORT DOCUMENTATION PAGE

Form Approved
OMB No. 0704-0188

Public reporting burden for this collection of information is estimated to average 1 hour per response, including the time for reviewing instructions, searching existing data sources, gathering and maintaining the data needed, and completing and reviewing this collection of information. Send comments regarding this burden estimate or any other aspect of this collection of information, including suggestions for reducing this burden to Department of Defense, Washington Headquarters Services, Directorate for Information Operations and Reports (0704-0188), 1215 Jefferson Davis Highway, Suite 1204, Arlington, VA 22202-4302. Respondents should be aware that notwithstanding any other provision of law, no person shall be subject to any penalty for failing to comply with a collection of information if it does not display a currently valid OMB control number. **PLEASE DO NOT RETURN YOUR FORM TO THE ABOVE ADDRESS.**

1. REPORT DATE *(DD-MM-YYYY)*	2. REPORT TYPE	3. DATES COVERED *(From - To)*
	Final Technical Report	01/06/10-01/06/12

4. TITLE AND SUBTITLE
High Performance InGaN-Based Solar Cells

5a. CONTRACT NUMBER

5b. GRANT NUMBER
HR0011-10-1-0049

5c. PROGRAM ELEMENT NUMBER

6. AUTHOR(S)
Speck, James; DenBaars, Steven; Mishra, Umesh; Nakamura, Shuji

5d. PROJECT NUMBER

5e. TASK NUMBER

5f. WORK UNIT NUMBER

7. PERFORMING ORGANIZATION NAME(S) AND ADDRESS(ES)
University of California, Santa Barbara
3227 Cheadle Hall
Santa Barbara, CA 93106-2050

8. PERFORMING ORGANIZATION REPORT NUMBER

9. SPONSORING / MONITORING AGENCY NAME(S) AND ADDRESS(ES)
Defense Advanced Research Projects Agency
3701 North Fairfax Drive

10. SPONSOR/MONITOR'S ACRONYM(S)
DARPA

11. SPONSOR/MONITOR'S REPORT NUMBER(S)

12. DISTRIBUTION / AVAILABILITY STATEMENT
"Approved for Public Release, Distribution is Unlimited"

13. SUPPLEMENTARY NOTES

14. ABSTRACT

Recent work has focused on exploring new solar cell designs more conducive to reaching higher indium contents in our InGaN-based active regions to extend the spectral response of our devices out to longer wavelength. This works includes testing devices with new multiple double heterostructure (MDH) and multiple quantum well (MQW) active region designs instead of our previous single double heterostructure (SDH) active region designs; investigating the growth conditions needed to reach longer emission and absorption wavelengths in our active regions; optimizing our p-GaN growth conditions to improve surface morphology, contact resistance, and carrier extraction; investigating the properties of solar cells grown by NH3-based molecular beam epitaxy (MBE); measuring the relationship between light absorption and external quantum efficiency (EQE) for our solar cells; increasing the total absorption in our solar cells by using light coupling with photonic crystals (PhCs); increasing the total absorption in our solar cells by using surface roughening; and finally increasing the total absorption in our solar cells by using anti-reflective (AR) coatings on the top sides of our devices and high-reflectivity (HR) coatings on the back sides of our devices

15. SUBJECT TERMS
Solar cells, InGaN, radiation hard, short wavelength, multijunction solar cells, high temperature operation

16. SECURITY CLASSIFICATION OF:			17. LIMITATION OF ABSTRACT	18. NUMBER OF PAGES	19a. NAME OF RESPONSIBLE PERSON
a. REPORT	b. ABSTRACT	c. THIS PAGE			James Speck
U	U	U	SAR	77	19b. TELEPHONE NUMBER *(include area code)* 805-893-8005

Standard Form 298 (Rev. 8-98)
ISI Std. Z39.18

20120607053

Final Technical Report

DARPA Program for
High Performance InGaN-Based Solar Cells

05/12/2012

Lead Organization: University of California, Santa Barbara
Type of Business: Other Educational

PI: James S. Speck
PI: Steven P. DenBaars
PI: Umesh K. Mishra
PI: Shuji Nakamura

Materials Department
Department of Electrical and Computer Engineering
University of California
Santa Barbara, CA 93106

Summary

This document summarizes the work that was performed for the High Performance InGaN-Based Solar Cell Project. Section 1 discusses our device development strategy and summarizes the key steps that were necessary to extend the absorption edge of InGaN-based solar cells to longer wavelengths. Sections 2 through 4 then describe the effects of doping, well width, and polarization on carrier collection for solar cells with relatively low indium content active regions (e.g. $x<0.15$ in $In_xGa_{1-x}N$). Screening polarization charges by delta doping on either side of the active region is demonstrated to be an essential strategy for efficient carrier collection. Sections 5 through 7 then discuss the development of the growth conditions that are necessary for creating high-performance devices with high indium content quantum wells (QWs) (e.g. $x>0.15$ in $In_xGa_{1-x}N$). The effects of the number of the QWs on carrier collection and the effects of surface roughening on device performance are also discussed. Building on these advances, the unique thermal properties of high indium content multiple quantum well (MQW) solar cells are examined in Section 8.

Section 9 then discusses how to best integrate InGaN-based solar cells with GaAs-based multijunction solar cells. These calculations suggest that it makes the most sense to integrate InGaN-based solar cells with four junction (as opposed to the more common three junction) GaAs-based solar cells and that the optimum bandgap of integrated InGaN-based cells should be around 2.65 eV. These calculations also show that it will be necessary to use high-performance broadband optical coatings to reduce unwanted reflections at the top interface and the bonding interfaces of any hybrid bonded cell design. Section 10 then discusses the demonstration and application of broadband optical coatings to InGaN-based solar cells.

Section 11 then examines the relationship between QW composition and device performance for Ga-polar *c*-plane solar cells. These results show that device performance degrades significantly with increasing QW indium content for devices with relatively wide barriers. Suspecting that polarization may play a role, these studies led us to investigate semipolar solar cells, as discussed in Sections 12 through 14. However, as discussed in Section 12, the growth of semipolar solar cells with a large number of periods was limited by the relatively high background oxygen concentrations (~1E17 cm^{-3}) in semipolar active regions compared to Ga-polar *c*-plane active regions (~1E16 cm^{-3}). In addition, it was found that the performance of semipolar solar cells showed little improvement over the performance of Ga-

polar *c*-plane solar cells with increasing QW indium content. Suspecting that our devices were limited by thermionic emission out of the QWs and not by polarization, these results led us to grow a series of devices with varying barrier width and relatively high indium content. Indeed, the devices with thinner barriers performed much better than the devices with thicker barriers, suggesting that interwell tunneling is essential for carrier transport in devices with relatively high indium content QWs. However, when we tried to grow devices with thin barriers with a larger number of periods (e.g. >20X), a high density of both basal-plane and non-basal-plane MDs formed due to the nonzero resolved stresses on the multiple glide planes present for semipolar orientations, thus ruining device performance. In contrast, the *c*-plane growth orientation has a no resolved stresses on the glide-dominant basal plane and it has relatively low oxygen incorporation, thus avoiding both of the major problems associated with growth on semipolar planes. Thus, it is our conclusion that the most promising path forward is to try to grow Ga-polar *c*-plane InGaN solar cells with thin barriers and a high number of periods. Although this approach should be limited by the formation of v-defects for devices with thin barriers grown on sapphire, this problem can be circumvented by growing devices on free-standing Ga-polar *c*-plane substrates with a low density of threading dislocations.

1. Development Strategy and Device Progress Timeline

III-nitride semiconductors are unique among common solar cell materials in that large polarization charges exist at the heterointerfaces. These charges arise from discontinuities in spontaneous polarization and strain-induced piezoelectric polarization. The spontaneous and piezoelectric polarization sheet charges can be very large and result in high internal electric fields greater than 1 MV/cm. If not properly taken into account, these polarization fields can adversely affect device performance. In previous reports, we showed how doping can be used to effectively screen the polarization fields and markedly improve device performance, effectively eliminating the "kinks" commonly observed in current-voltage (I-V) curves for InGaN-based solar cells.

These studies on screening polarization fields formed the basis of strategy for developing InGaN-based solar cells with high indium content QWs, which is depicted in the flow chart in Fig. 1.1. In addition to understanding how doping can be used to screen polarization fields, we have discovered that decreasing the well thickness can also have the effect of screening the polarization fields in the active region. This has resulted in a transition from bulk p-i-n to multiple double heterostructure (MDH) to MQW active regions designs and will be presented in Section 4. Then, in Section 5, we will present progress in the growth conditions for high indium content QWs and discuss how the number of QWs affects device performance. Next, in Sections 6 and 7, we will demonstrate how incorporating intentionally surface roughening can affect device

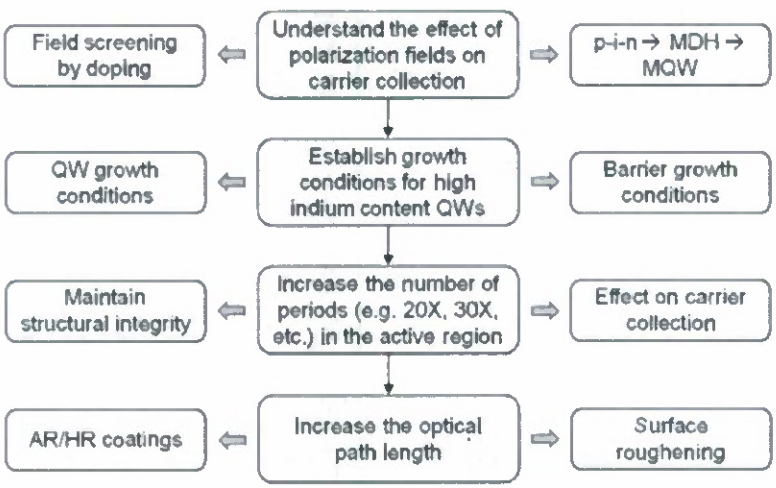

Fig. 1.1. Flow chart illustrating the strategy for developing InGaN-based solar cells with high indium content QWs.

(a)

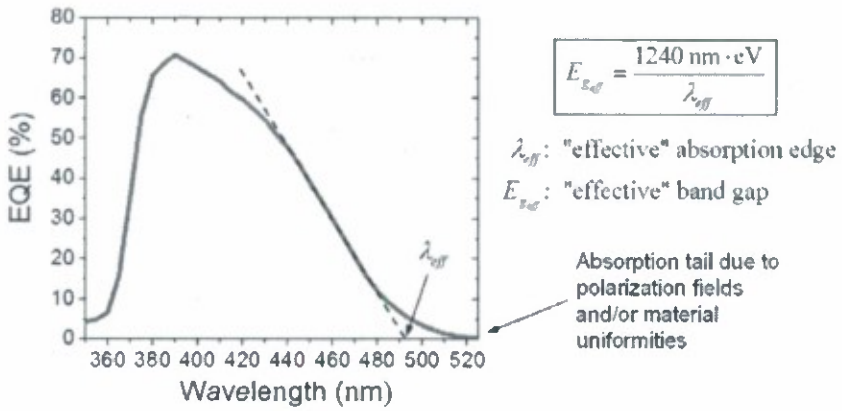

(b)

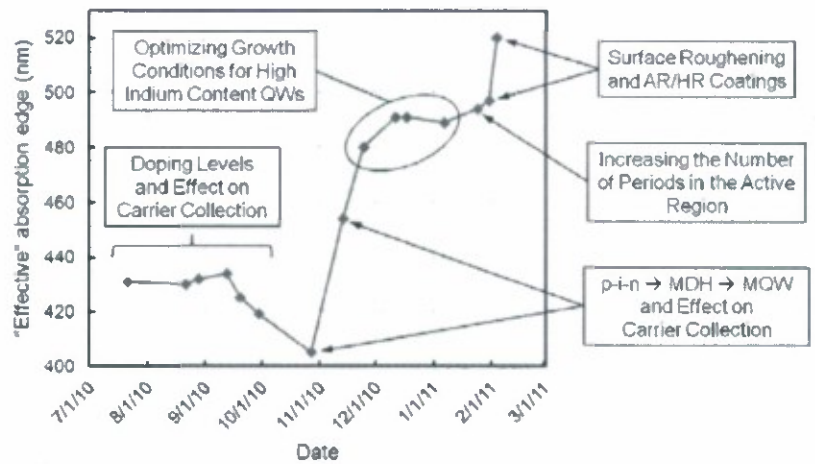

Fig. 1.2. (a) Typical plot of the dependence of EQE on wavelength for an InGaN-based solar cell illustrating the definition of "effective" absorption edge and "effective" band gap in the presence of polarization fields. (b) Timeline showing the progression of the "effective" absorption edge for InGaN-based solar cells during the last 6 months of 2010 and the first two months of 2011.

performance. Finally, in Section 8, we will examine the thermal performance of high indium content MQW solar cells.

As a metric for tracking our device progress over time we have defined a new quantity which we refer to as the "effective" absorption edge. The definition of this quantity is illustrated in Fig. 1.2(a), which shows a typical plot of the dependence of external quantum efficiency (EQE) on wavelength for an InGaN-based solar cell. Aside from the absorption tail, which is always present and is most likely due to polarization fields and/or material nonuniformities, the spectral response typically exhibits a linear decrease in EQE with wavelength near the material band gap. Neglecting the absorption tail, we define the x-intercept of this linear decrease in EQE

with wavelength as the "effective" absorption edge, or λ_{eff}. From the "effective" absorption edge, we can also define an "effective" band gap as

$$E_{g_{eff}} = \frac{1240\ nm \cdot eV}{\lambda_{eff}}. \tag{1.1}$$

Although we define these quantities for the sake of tracking device progress, we refrain from referring to the "effective" absorption edge or the "effective" band gap as the actual absorption edge or band gap, as the presence of strong electric fields can have a significant effect on the absorption spectra of a material. Future studies will focus on determining the actual absorption edge and band gap of our solar cells.

The timeline in Fig. 1.2(b) shows the progression of the "effective" absorption edge for our solar cells during the last 6 months of 2010 and the first 2 months of 2011. As illustrated in the timeline, understanding how to screen the polarization fields by doping and decreasing well width formed the basis for extending the "effective" absorption edge of our devices to longer wavelengths. Following these breakthroughs in an understanding of the device physics, our effective absorption edge rapidly increased from ~405 nm at the end of October 2010 to ~520 nm at the beginning of February 2011.

Following a rapid increase in effective absorption edge during the end of 2010 and beginning of 2011, we devoted some effort to determine how to best integrate InGaN-based solar cells with GaAs-based multijunction solar cells. These calculations, which are presented in Section 9 and 10, suggest that it makes the most sense to integrate InGaN-based solar cells with four junction (as opposed to the more common three junction) GaAs-based solar cells and that the optimum bandgap of integrated InGaN-based cells should be around 2.65 eV (corresponding to $\lambda \sim 465$ nm), indicating that we should focus on making high-performance InGaN solar cells at slightly shorter wavelengths than originally intended. Thus, the focus of the work presented in Sections 11 through 14 was shifted from determining how to increase absorption edge to determining how to improve solar cell performance at 2.65 eV. This led us to make a thorough comparison of Ga-polar *c*-plane and semipolar solar cells, as discussed in detail in Sections 11 through 14.

2. Effect of n-type and p-type Doping Levels on Carrier Collection

III-nitride semiconductors are unique among common solar cell materials in that large polarization charges exist at the heterointerfaces. These charges arise from discontinuities in spontaneous polarization and strain-induced piezoelectric polarization. The spontaneous and piezoelectric polarization sheet charges can be very large and result in high internal electric fields of 1 MV/cm. If not properly taken into account adverse device performance can result. To understand the possible effects of polarization on an InGaN/GaN solar cell the energy band

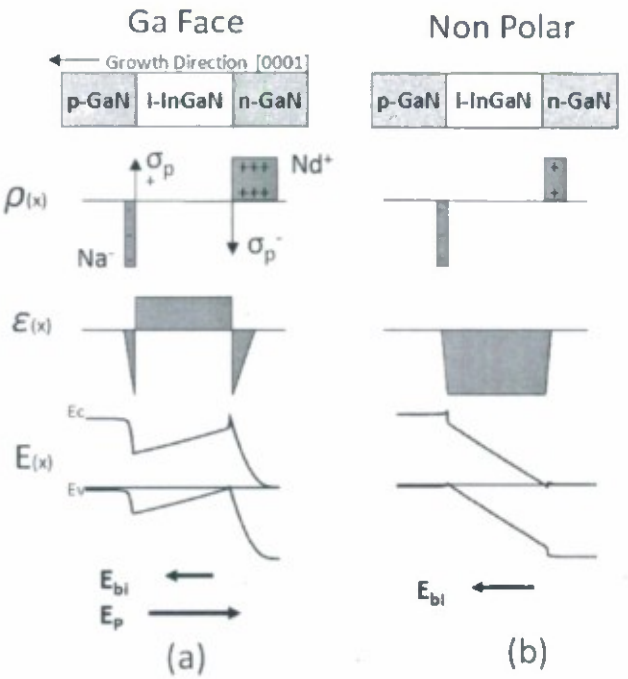

Fig. 2.1. Device structure, charge distribution, electric field distribution, end energy band diagram for an InGaN/GaN double heterostructure (DH) solar cells with X_{In}=.24 for (a) standard Ga-face polar orientation and (b) without polarization.

diagram must be compared for a device with and without polarization. Figure 2.1 shows the charge and electric field distribution and energy band diagram for a GaN/InGaN/GaN double heterostructure (DH) solar cell both (a) with and (b) without polarization for an In composition of 24%. It is clear from Fig. 2.1(a) that the polarization sheet charges (σ_p) induce a dipole which, in this case, switches the direction of the electric field in the InGaN layer. This means that any carriers that are generated in the InGaN layer will be forced in the opposite direction needed for

carrier collection, and they will likely recombine resulting in a reduction in the photogenerated current and the EQE. The two major factors that determine the direction and magnitude of the electric field in the InGaN layer are the InGaN composition and doping density in both the p-GaN and n-GaN. The InGaN composition determines the magnitude of the polarization sheet charges which, for a given In composition and device structure, are constant. In contrast, though, the doping densities can be varied for a given device structure. The energy band diagram for an InGaN/GaN DH and an MDH solar cell with various levels of Si doping on the n-GaN side of the junction are shown in Fig. 2.2. Note that the electric field magnitude and direction in the InGaN layer is quite sensitive to the doping level. Similar arguments hold for MDH and MQW structures. If the doping is too low (as is the case for the Si concentration of $2x10^{18}$ cm^{-3} in Fig. 2.2(a) or $1x10^{18}$ cm^{-3} in Fig. 2.2(b)) then the

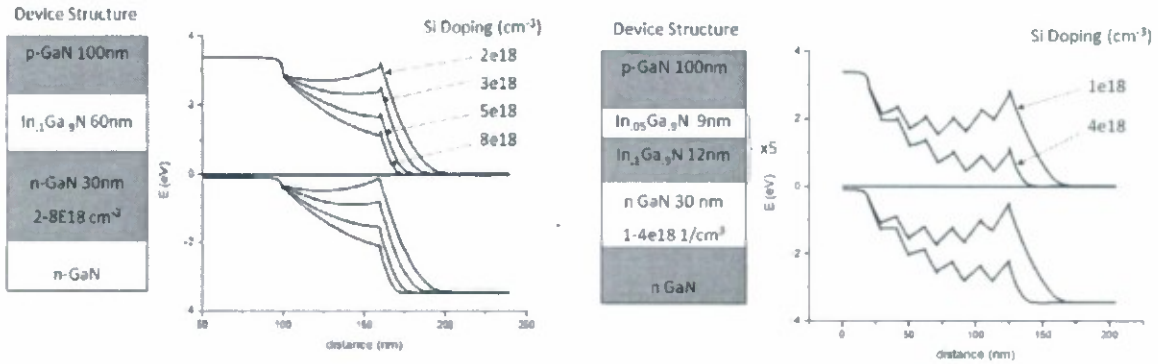

Fig. 2.2. Energy band diagram for InGaN/GaN (a) DH and (b) MDH solar cell with various Si doping levels.

polarization charges induce a field that creates a barrier to electrons and holes from being swept from the InGaN region. The doping density on the n and p sides must be carefully chosen for optimal device performance.

To study the effects of the polarization induced fields a series of devices were grown with n-GaN layers with various Si concentrations. The devices were grown on 50 mm sapphire substrates and consisted of a 4 μm thick GaN template with Si concentration of $4.5x10^{18}$ cm^{-3}, a 0.2 μm Si doped layer with concentration raging from $6x10^{17}$ cm^{-3} to $6.8x10^{18}$ cm^{-3}, an InGaN MDH structure consisting of 5 periods of 12nm $In_{0.12}Ga_{0.88}N$ wells and 9 nm $In_{0.05}Ga_{0.95}N$ barriers, and a 60 nm thick p-GaN layer with a Cp_2Mg flow of 10 sccm. The devices were

fabricated into 1 mm x 1 mm mesas with a Pd/Au grid contact to the p-GaN with a grid spacing of 200 μm and Al/Au contact to the n-GaN layer. The resulting current density-voltage (*J-V*) and EQE data for the sample with Si concentration of $6x10^{17}$ cm^{-3} is shown in Figs. 2.3(a) and 2.3(b), respectively. The illuminated *J-V* curve shows a kink with a knee voltage (V_k) at approximately -3.4 V which indicates the onset of a reduction in photocurrent due to suppressed carrier collection. V_k is defined as the intercept of the linear part of the J-V curve after initial turn-on with the extrapolation of the saturated (constant) portion of photogenerated current in reverse bias (see Fig. 2.3(a)). EQE measurements were taken at bias voltages both below and above V_k at -4 V and 0 V respectively. Figure 2.3(b) shows the EQE spectra taken at 0 V (solid line) indicating no spectral response beyond the GaN band edge at 360 nm suggesting that any carriers generated in the InGaN region were not being collected and were recombining due to an insufficient electric field. This behavior is consistent with the conjecture that the lightly doped n-GaN resulted in a flattening of

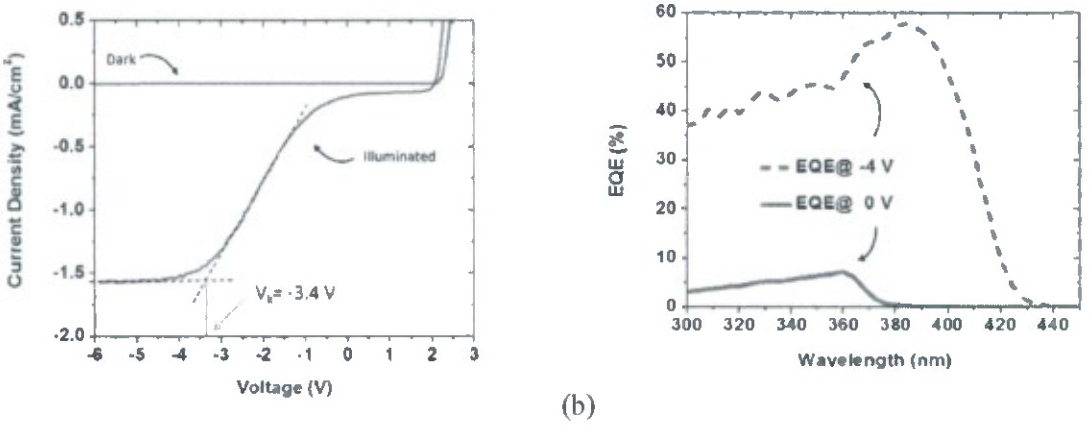

(a) (b)

Fig. 2.3. (a) Dark and illuminated current density vs. voltage showing the knee voltage (V_k) and (b) EQE vs. wavelength measured at 0 V and -4 V for an InGaN/GaN MDH device with Si concentration in the n-GaN layer of $6x10^{17}$ cm^{-3}.

the bands in the InGaN layer and that, without a field to sweep carriers out of the depletion region, there was no carrier collection. The dashed line in Fig. 2.3(b) corresponds to the EQE spectra taken at -4 V reverse bias and shows significant spectral response out to the InGaN band edge at 425 nm. This measurement indicates that by reverse biasing the device sufficiently (beyond V_k) we can induce a large enough electric field across the InGaN region to effectively

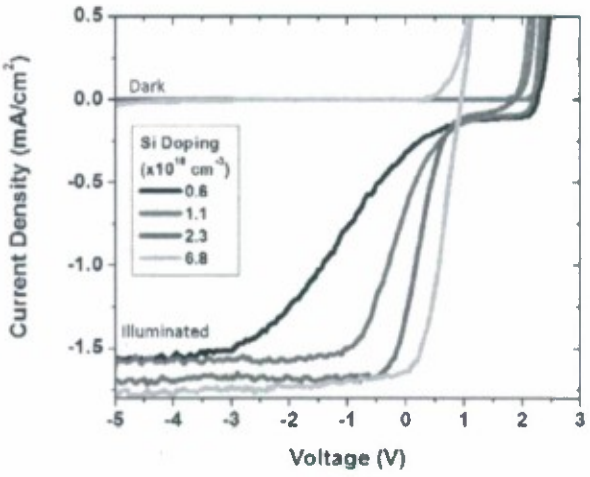

Fig. 2.4. Dark and illuminated current density vs. voltage for InGaN/GaN MDH devices with Si concentration of 0.6-6.8x10^{18} cm^{-3} in the n-GaN and Cp_2Mg flow of 10 sccm in the p-GaN.

collect carriers generated in the InGaN region. The knee voltage is therefore an approximate measure of how much applied voltage is required to induce an electric field in the InGaN region and will depend on the equilibrium band bending in the InGaN region which depends on doping and In composition. Increasing the doping in the n-GaN should shift V_k to positive voltages and eliminate the kink in the J-V curve all together. Representative dark and illuminated *J-V* curves for the devices with various Si doping are shown in Fig. 2.4. Note that the knee voltage moves from -3 V for the lowest Si doping to above 0 V for the higher doping and the kink is completely eliminated. However, the Voc for the device with the highest Si doping of 6.8x10^{18} cm^{-3} drops to 1 V as compared to the approximately 2 V for the devices with lower doping. Similar low Vocs we observed for all devices with Si doping greater than 5x10^{18} cm^{-3}. This indicates that while carrier collection is not a problem at zero bias in devices with higher doping levels there is a problem with generating photocurrent in forward bias in devices with higher doping levels and is a topic of further investigation.

We have shown that low n-type doping can lead to non-ideal device behavior due to a polarization induced reduction of the electric field in the InGaN region, but low p-type doping can also cause similar problems. According to simulations the doping in our p-GaN (Mg concentration ~5x10^{19} cm^{-3}) in standard structures should be

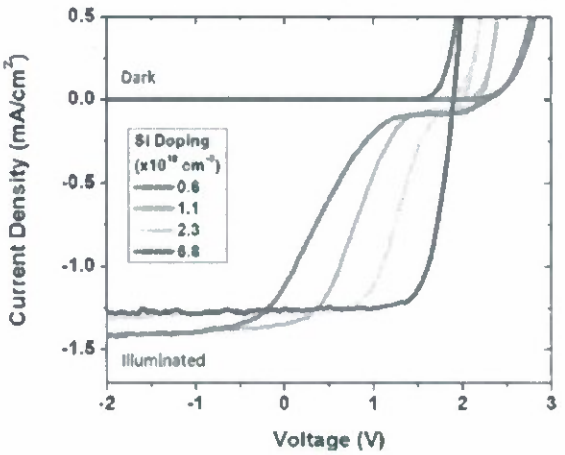

Fig. 2.5. Dark and illuminated current density vs. voltage for InGaN/GaN MDH devices with Si concentration of 0.6-6.8x10^{18} cm^{-3} in the n-GaN and a 2-step Cp_2Mg flow of 50/10 sccm in the p-GaN.

high enough to ensure there is a strong field in the InGaN. Despite these simulations, though, we have still observed problems with carrier collection in our standard structures. One possible source of an unintended reduction in p-type doping is a well documented lag between Cp_2Mg flow and Mg incorporation in growth of p-GaN by MOCVD. This lag in Mg incorporation results in a graded doping profile in which the Mg concentration is lowest near the junction. To counter this lag we repeated the previous experiment but with a two-step Mg doping profile where the first half of the p-GaN layer the Cp_2Mg flow is 50 sccm and then the flow is reduced to 10 sccm for the remainder of the layer. This should result in a sharper doping profile without the degradation associated with Mg over-doping such as reduced hole mobility and formation of inversion domains. The dark and illuminated *J-V* measurements for these devices are shown in Fig. 2.5. As expected, V_k shifted toward higher voltages for all devices compared to the lower p-type doping. Knee voltages ranged from -0.6 V for the device with 6x10^{17} cm^{-3} Si concentration to 1.5 V for the device with 6.8x10^{18} cm^{-3} Si concentration.

The relationship between knee voltage and Si doping is shown in Fig. 2.6 for both the single-step (10 sccm) and two-step (50/10 sccm) Cp_2Mg flow scheme. Both curves follow a similar trend of increasing V_k with higher Si-doping, but the two-step Mg doping results in a significant positive shift in the knee voltage for each Si concentration. The device with 50/10 sccm Cp_2Mg and 6.8x10^{18} cm^{-3} Si had a Voc of 1.9 V and FF of 71% making it one of the best performing devices in the literature at this In composition. Based on this experiment we also

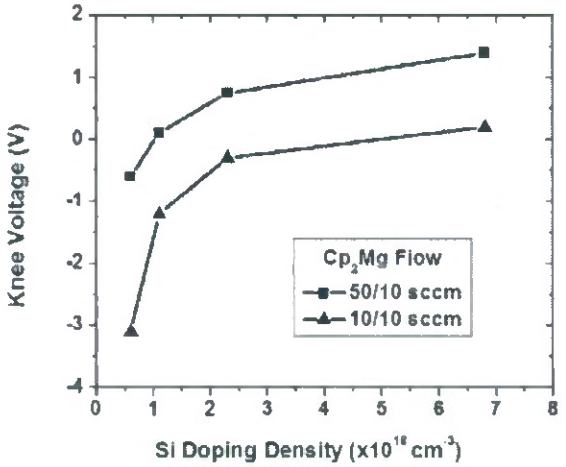

Fig. 2.6. Knee voltage (V_k) vs. Si concentration for devices with Cp_2Mg flow of 50/10 sccm (■) and 10/10 sccm (▲).

learned that we can reduce the first Cp_2Mg flow and achieve even higher device performance. Fig. 2.7 shows an illuminated *J-V* curve for a MDH device with optimized doping of $6.8x10^{18}$ cm^{-3} Si and a two-step Cp_2Mg flow of 20/10 sccm. This device had a Voc of 1.9 V and a FF of 77%.

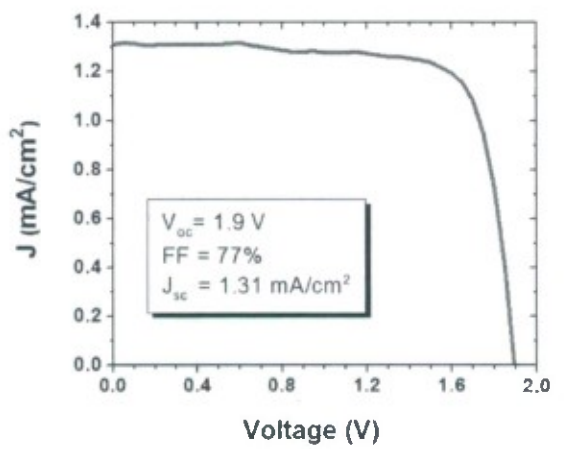

Fig. 2.7. Illuminated current density vs. voltage for InGaN/GaN MDH solar cell with optimized doping. Si = $6.8x10^{18}$ cm^{-3} and two-step p-type doping (Cp2Mg = 20/10 sccm).

As we move to higher In content devices we will have to continue to manage the effects polarization. This work provides a framework which properly takes into account the polarization-induced electric fields and can be used to design high performance III-nitride solar cells.

3. Multiple Double Heterostructure Solar Cells

We have previously focused on p-i-n solar cell structures that work well for relatively low indium content InGaN devices. However, as the absorption edge of our InGaN solar cells are pushed from the blue to the green portion of the solar spectrum, practical limitations are becoming more apparent. At high indium compositions, the critical thickness limit in epitaxial growth is well below the thickness needed for full optical absorption using standard device designs. To address these issues, we are exploring MDH active region designs, which are similar to MQW regions in standard light-emitting diode (LED) structures, but with thicker wells to increase the optical absorption. For the purposes of clarity, we define a QW as being less than 10 nm thick and DH as being greater than 10 nm thick. Figure 3.1 shows cross-sectional schematics of the two types of solar cells discussed below: (a) standard p-i-n solar cell designs and (b) new MDH solar cell designs. Both solar cell structures were grown by metalorganic chemical vapor deposition (MOCVD) and consisted of double-side polished (DSP) sapphire substrates, 1300 nm undoped GaN templates, 700 nm Si-doped n-GaN layers, varying undoped InGaN-based active regions, and 300 nm Mg-doped p-GaN layers. The active regions of the p-i-n solar cells consisted of a single 60 to 105 nm thick InGaN layer, while the active regions of the MDH solar cells consisted of 9 nm $In_yGa_{1-y}N$ barriers and 12 nm $In_xGa_{1-x}N$ wells, repeated 5 times. The nominal composition of the high indium content layers was $In_{0.10}Ga_{0.90}N$, as verified by x-ray diffraction (XRD).

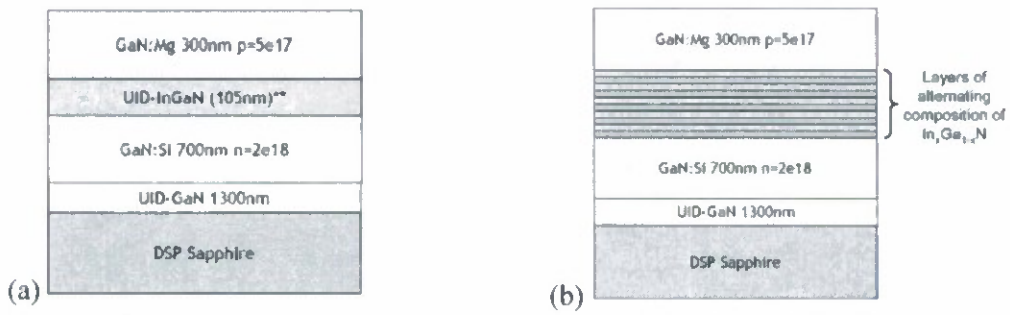

Fig. 3.1. (a) Schematic of an p-i-n solar cell. (b) Schematic of an MDH solar cell with alternating compositions of $In_xGa_{1-x}N$. **The thickness of the active region of the solar cell varies depending on the sample.

A direct comparison (Fig. 3.2) of a p-i-n solar cell with a 60 nm InGaN active region to an MDH solar cell with GaN barriers (GB-MDH) showed that the peak EQEs were comparable and primarily dependent on the total thickness of the InGaN layers, which was the same for both structures. The 60 nm p-i-n solar cell had EQE values of 79% at 382 nm and 50% at 413 nm, while the GB-MDH solar cell had EQE values of 80% at 382 nm and 50% at 411 nm. The GB-MDH solar cell had a slightly higher open circuit voltage (V_{oc} = 1.95 V) than the 60 nm p-i-n solar cell (1.90 V). This can possibly be attributed to lower leakage in the GB-MDH design because of the lower probability of generating misfit dislocations in thinner InGaN layers. In addition, we observed slightly lower fill factors (FFs) for the GB-MDH solar cell (60.7%) than the 60 nm p-i-n solar cell (75%), which may be due to increased series resistance from the additional heterointerfaces in the active region.

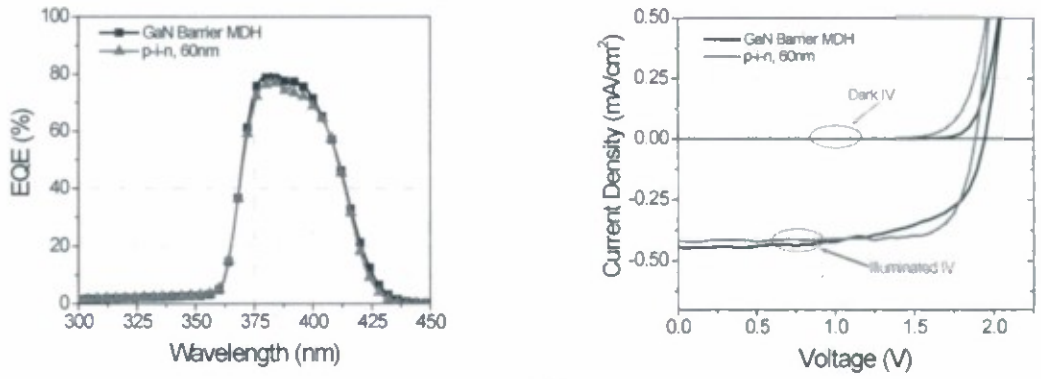

(a) (b)

Fig. 3.2. (a) Comparison of the EQE spectra of the 60 nm p-i-n solar cell with the GB-MDH solar cell. (b) Comparison of the I-V characteristics of the 60 nm p-i-n solar cell with the GB-MDH solar cell.

The effect of barrier composition on solar cell performance was also investigated. MDH solar cells with 9 nm $In_yGa_{1-y}N$ barriers and 12nm $In_xGa_{1-x}N$ wells (IB-MDHs) were grown for comparison with the 60 nm p-i-n and GB-MDH solar cells. For the IB-MDH solar cells, the indium composition in the barriers was about one third the indium composition in the wells. Figure 3.3 shows the EQE spectra and the *J-V* characteristics for the IB-MDH solar cell and an p-i-n solar cell with a 105 nm InGaN active region. Compared to the 60 nm p-i-n solar cell and the GB-MDH solar cell, the peak EQE of the 105 nm p-i-n solar cell and the IB-MDH solar cell increased by about 10%. This increase in peak EQE was attributed to the increase in total InGaN

thickness in the active regions of the devices, which contained a total of 105 nm of InGaN as opposed to 60 nm of InGaN for the GB-MDH solar cell and the 60 nm p-i-n solar cell. Much like the 60 nm p-i-n solar cell and GB-MDH solar cell, the peak EQEs of the 105 nm p-i-n solar cell and the IB-MDH solar cell were comparable and appeared to depend primarily on the total thickness of InGaN in the active region. In addition, compared to the 105 nm p-i-n solar cell, the IB-MDH solar cell did not show a decrease in FF, unlike the decrease in FF for the GB-MDH solar cells compared to the 65 nm p-i-n solar cell. This can be attributed to a reduction in the heterointerface barrier height for the IB-MDH solar cell compared to the GB-MDH solar cell. These results indicate that by introducing multiple interfaces into the active region of our solar cells we can potentially achieve much higher indium content absorbing regions than possible with p-i-n designs, without compromising electronic properties.

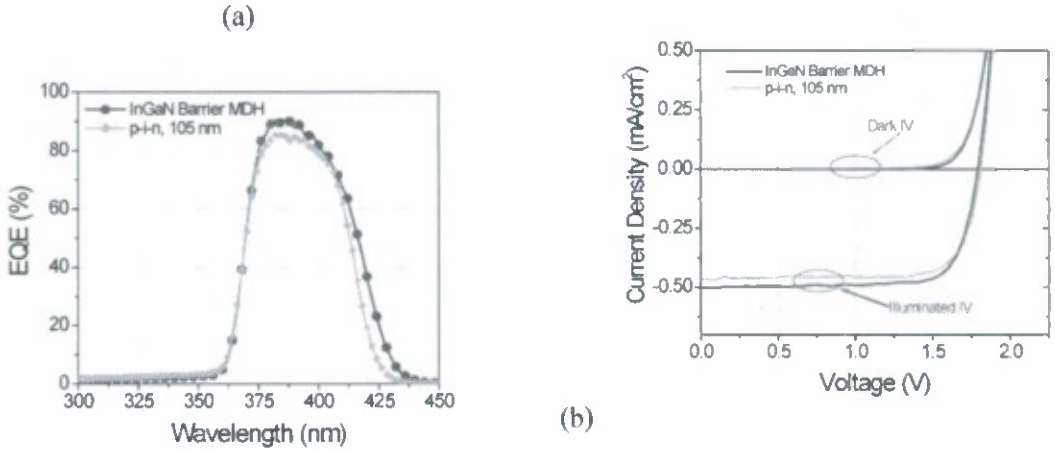

Fig. 3.3. (a) Comparison of the EQE spectra of the 105 nm p-i-n solar cell with the IB-MDH solar cell. (b) Comparison of the I-V characteristics of the 105 nm p-i-n solar cell with the IB-MDH solar cell.

4. Effect of QW Thickness on Carrier Collection

As we progress toward solar cells with higher indium content active layers it is necessary to decrease the thickness of the active layers to account for increases in misfit strain. Although our device design was initially driven by materials-related constraints, we have discovered recently that fabricating devices with thinner active layers can have additional benefits related to screening polarization fields. Figure 4.1(a) shows a cross-sectional schematic of the epitaxial structure of a series of devices with varying well widths. The devices were grown by MOCVD on 50 mm double-side-polished sapphire substrates and consisted of a 3 μm n-GaN template, an undoped InGaN-based active region, and a 75 nm p-GaN layer. The active regions varied between the devices and consisted of 60 nm total $In_{0.07}Ga_{0.93}N$ with 5 nm GaN barriers and varying thickness $In_{0.07}Ga_{0.93}N$ "wells." The final device structure consisted of 1 mm x 1 mm mesas for confining the current flow through the p-GaN, Pd/Au p-contact grids on the top of each mesa with a center-to-center grid spacing of 200 μm, and Al/Au n-contacts around the base of each mesa.

Figure 4.1(b) shows the dependence of EQE on wavelength with varying well width. Considering that the EQE was nearly identical for all of the devices, the introduction of thin QWs and additional heterobarriers did not appear to decrease the absorption edge or reduce the carrier collection efficiency. As shown in Fig. 4.2(a), decreasing the well width also eliminated the "kink" in the *J-V* curve that was present for devices with wider wells. In addition, the fill factor and open-circuit voltage increased with decreasing well

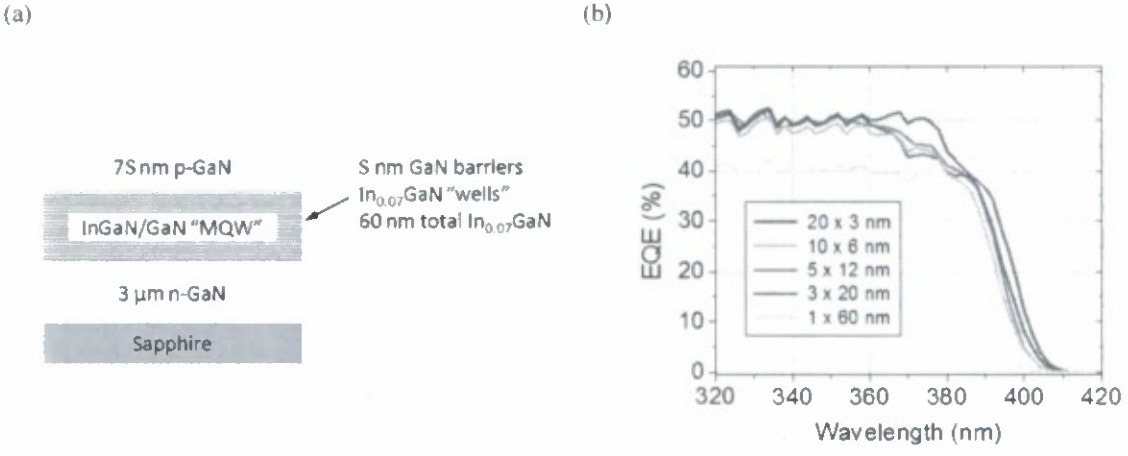

Fig. 4.1. (a) Cross-sectional schematic of the epitaxial structure of a series of devices with varying well widths. (b) Dependence of EQE on wavelength with varying well width.

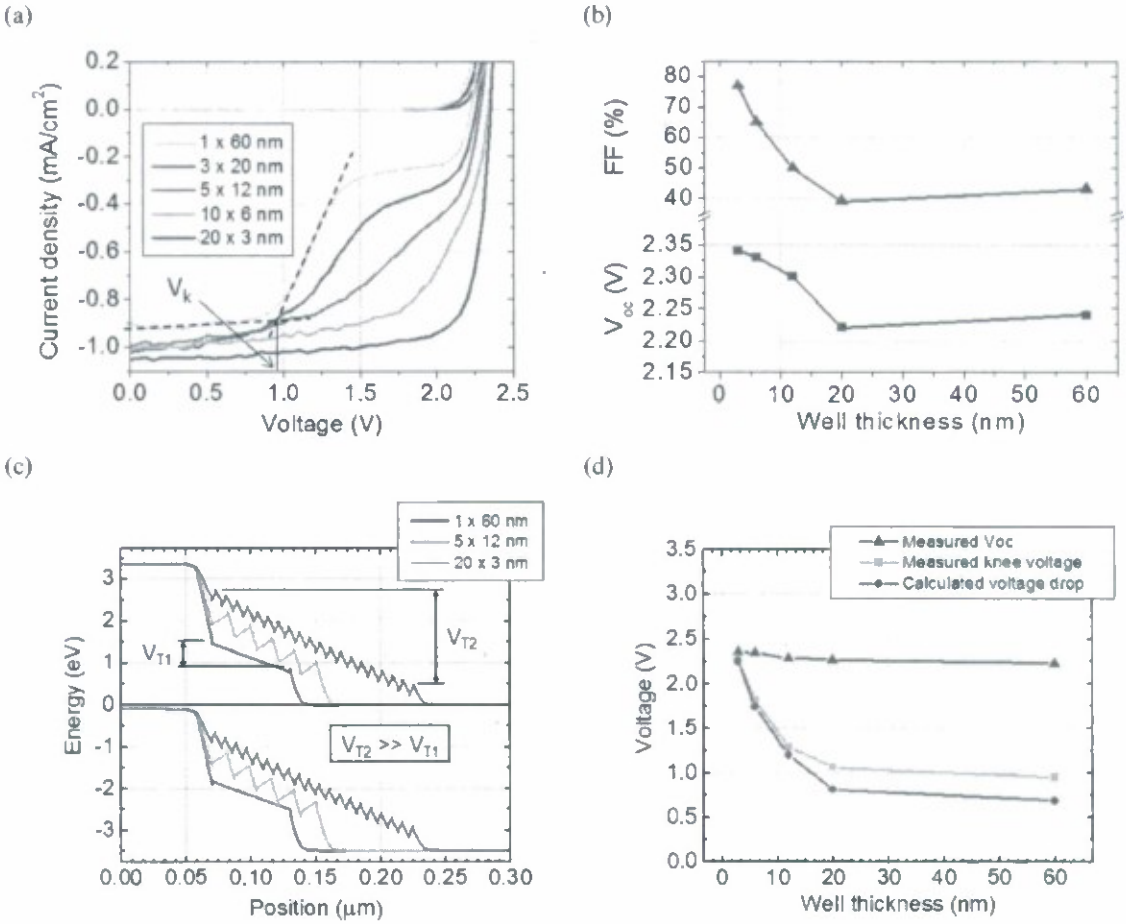

Fig. 4.2. (a) Dependence of dark and illuminated current density on voltage for the series of devices depicted in Fig. 3. (b) Dependence of fill factor and open-circuit voltage on well thickness. (c) Calculated energy band diagrams for a series of devices with varying well thickness. (d) Dependence of measured open-circuit voltage, measured knee voltage, and calculated voltage drop on well thickness.

thickness, as indicated in Fig. 4.2(b).

To understand the physical relationship between these observations and well width, Fig. 4.2(c) shows calculated energy band diagrams under equilibrium for a series of devices with varying well width. As shown in the figure, the total voltage drop across the i-region under equilibrium, V_T, is much larger for the devices with thinner wells than for the devices with thicker wells. For the devices with thinner wells, the polarization sheet charges of the wells in the center of the active region screen one another, so only the thin wells at either end of the active region act to counter the built-in field of the p-n junction. Figure 4.2(d) summarizes the dependence of the measured open-circuit voltage, the measured knee voltage (V_k, see Fig.

4.2(a)), and the calculated total voltage drop on well thickness. Comparing this data to the *J-V* curves in Fig. 4.2(a), we see that if $V_T << V_{oc}$, the *J-V* curve has a kink and $V_k \sim V_T$. In contrast, if $V_T \sim V_{oc}$, the *J-V* curve is kink-free and the device operates as desired.

5. Optimizing Growth Conditions for High Indium Content QWs

Early attempts to grow InGaN-based solar cells with high indium content QWs were hindered by a limited understanding of the effects of polarization. Even after the effects of polarization were understood, though, there were still significant challenges remaining in developing the growth conditions for high indium content QWs. The lattice mismatch between InN and GaN is very large (~10%) and the optimal growth temperature of InGaN alloys is significantly lower than for GaN, making the growth of high indium content QWs very challenging. Figure 5.1(a) shows a cross-sectional schematic of the epitaxial structure of a series of devices with varying MQW growth temperatures. The devices were grown by MOCVD on 50

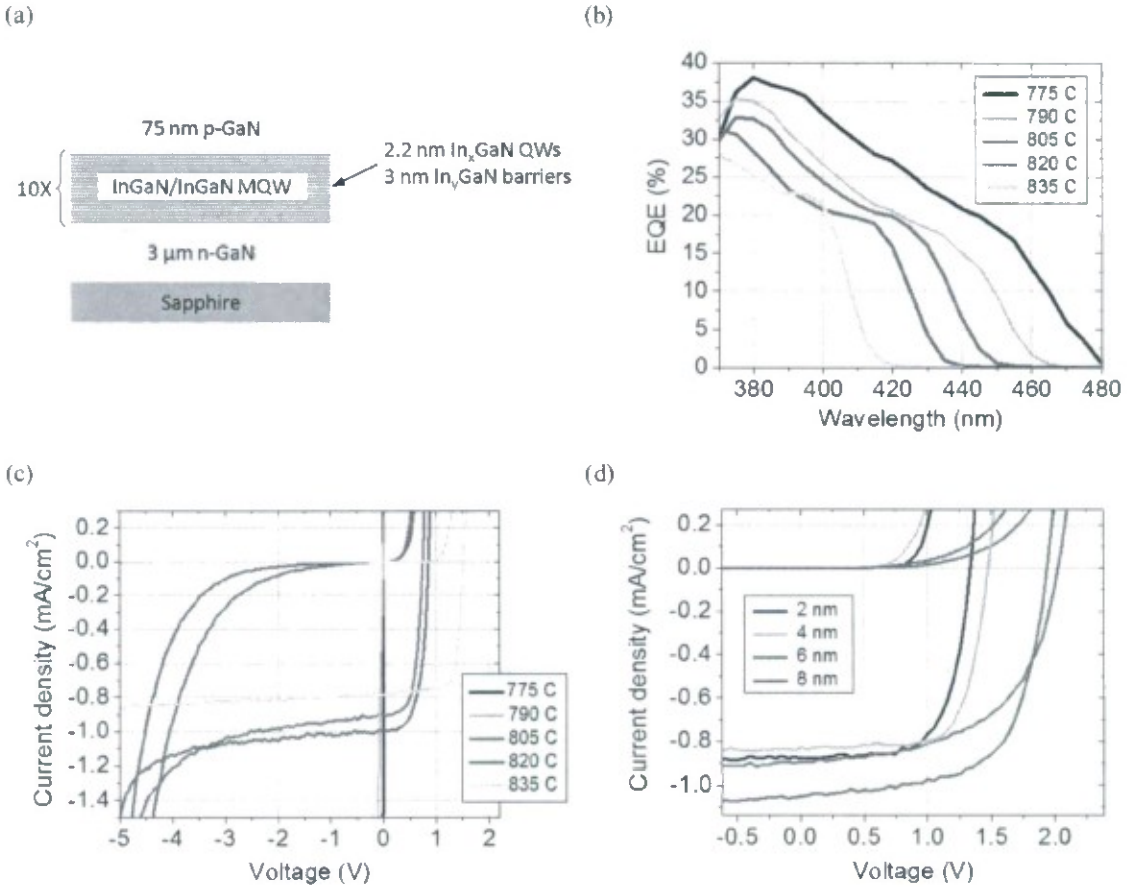

Fig. 5.1. (a) Cross-sectional schematic of the epitaxial structure of a series of devices with varying MQW growth temperatures. (b) Dependence of EQE on wavelength with varying MQW growth temperature. (c) Dependence of dark and illuminated current density on voltage with varying MQW growth temperature. (d) Dependence of dark and illuminated current density on voltage for a series of devices with a MQW growth temperature of 835 °C and varying barrier thicknesses.

mm double-side-polished sapphire substrates and consisted of a 3 μm n-GaN template, a 10 period 2.2/3.0 nm In_xGaN/In_yGaN MQW active region, and a 75 nm p-GaN layer. The growth temperature of the MQW was decreased from 835 to 775 °C in increments of 15 °C to increase the indium content of the MQW. The final device structure consisted of 1 mm x 1 mm mesas for confining the current flow through the p-GaN, Pd/Au p-contact grids on the top of each mesa with a center-to-center grid spacing of 200 μm, and Al/Au n-contacts around the base of each mesa. As shown in Fig. 5.1(b), the absorption edge increased monotonically with decreasing MQW growth temperature. However, as depicted in Fig. 5.1(c), as the growth temperature decreased and the indium content in the MQW increased, the devices became increasingly leaky. To determine the source of the leakage, a series of devices were grown with the same structure as in Fig. 5.1(a), but with a fixed MQW growth temperature of 835 °C and varying barrier widths. As depicted in Fig. 5.1(d), thicker barriers improved device performance by increasing the open-circuit voltage and decreasing the device leakage. However, since thick InGaN barriers would have added significantly to the accumulated stress in the MQW, all devices moving forward were grown with GaN barriers.

During our initial attempts to grow high indium content QWs we used very similar conditions for the growth of the QWs and barriers. These conditions included growing the barriers in the same carrier gas (i.e. N_2) and at the same temperature as the QWs. As time went on, though, it became clear that these conditions were not adequate, as significant surface pitting and leakage were present for all high indium content devices. To address these problems, a two-step barrier growth methodology, which is illustrated in Fig. 5.2(a), was developed. After growing the QWs in an N_2 carrier gas, a "cap" was grown in an N_2 carrier gas at the same temperature as the QWs. Following the growth of the cap, a GaN "barrier" was grown at elevated temperature in an H_2 carrier gas. The purpose of the high temperature barrier was to restore the growth morphology following the low temperature QW/cap growth and to suppress the formation of V-defects. Figure 5.2(a) shows a cross-sectional schematic of the epitaxial structure of a series of devices with varying cap thickness. The devices were grown by MOCVD on 50 mm double-side-polished sapphire substrates and consisted of a 3 μm n-GaN template, a 10 period 2.2/8.0 nm In_xGaN/GaN MQW active region, and a 75 nm p-GaN layer. The thickness of the caps varied from 2 to 4 nm and the thickness of the barriers varied from 4 to 6 nm, with

(a)

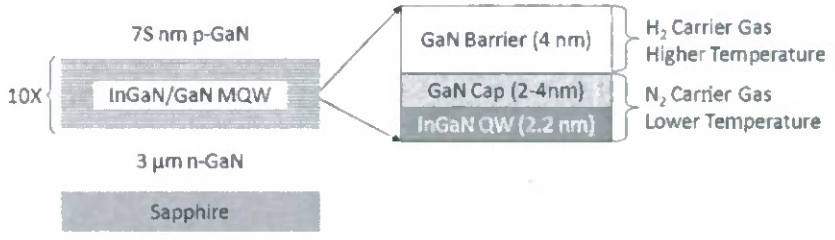

(b)

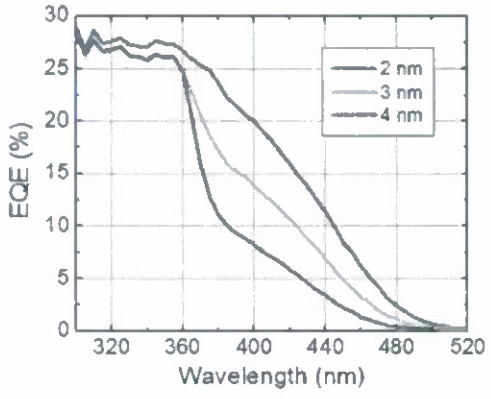

(c)

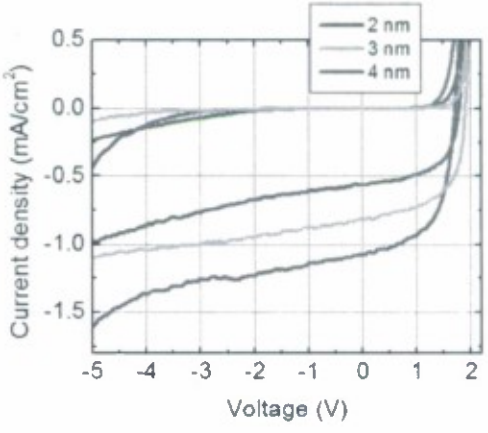

Fig. 5.2. (a) Cross-sectional schematic of the epitaxial structure of a series of devices with varying QW cap layer thicknesses. (b) Dependence of EQE on wavelength with varying QW cap layer thickness. (c) Dependence of dark and illuminated current density on voltage with varying QW cap layer thickness.

the total thickness of the cap plus barrier fixed at 8 nm. The growth temperature of the QWs and caps was 775 °C and the growth temperature of the barriers was 790 °C. The final device structure consisted of 1 mm x 1 mm mesas for confining the current flow through the p-GaN, Pd/Au p-contact grids on the top of each mesa with a center-to-center grid spacing of 200 μm, and Al/Au n-contacts around the base of each mesa. As shown in Figs. 5.2(b) and 5.2(c), the EQE and short-circuit current density decreased drastically for samples with thinner caps, suggesting that indium was desorbing from inadequately capped QWs during the growth of the barriers at elevated temperatures. These conclusions were also corroborated by XRD data (not shown), which confirmed that the average indium composition in the MQW decreased significantly with decreasing cap thickness.

Following the development of the two-step barrier process, additional studies were performed to further improve the morphology of the devices. Devices were grown by MOCVD

(a)

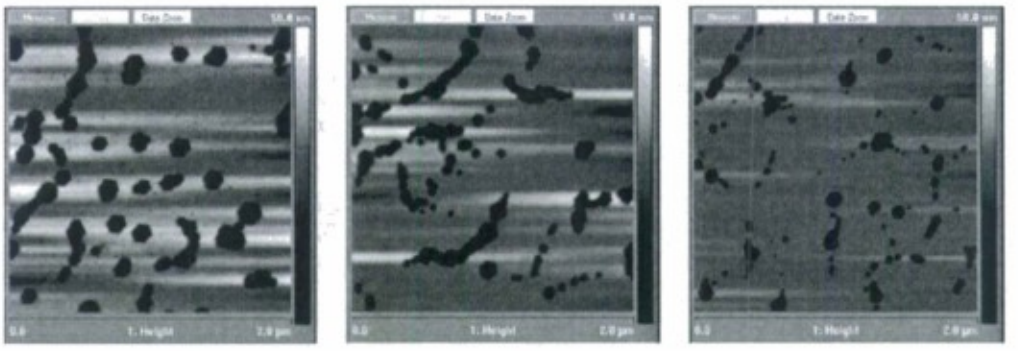

(b)

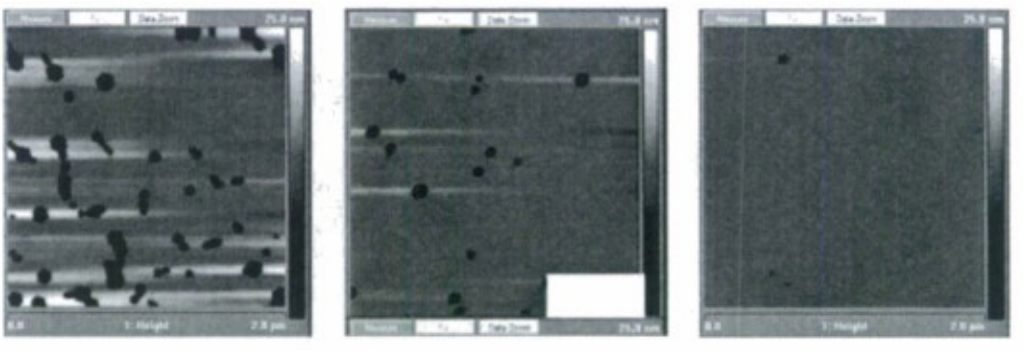

Fig. 5.3. (a) AFM images of a series of devices with varying barrier growth temperatures. (b) AFM images of a series of devices with varying p-GaN growth temperatures.

on 50 mm double-side-polished sapphire substrates and consisted of a 3 μm n-GaN template, a 10 period 2.2/8.0 nm In_xGaN/GaN MQW active region, and a 75 nm p-GaN layer. Figure 5.3(a) shows atomic force microscopy (AFM) images of three different devices with varying barrier growth temperatures (displayed below each image). The QW growth temperature and p-GaN growth temperature for all three devices were 765 and 850 °C, respectively. As indicated by the AFM data, the pit size and device leakage (data not shown) were reduced considerably with higher barrier growth temperatures. Despite these improvements, though, there were still pits present for all samples, as the p-GaN growth temperature was relatively low. Figure 5.3(b) shows AFM images of three different devices with varying p-GaN growth temperatures (displayed below each image). The QW growth temperature and barrier growth temperature for all three devices were 765 and 850 °C, respectively. As indicated by the AFM data, the higher

temperature p-GaN completely filled in the pits, further reducing the device leakage and improving the device performance (data not shown).

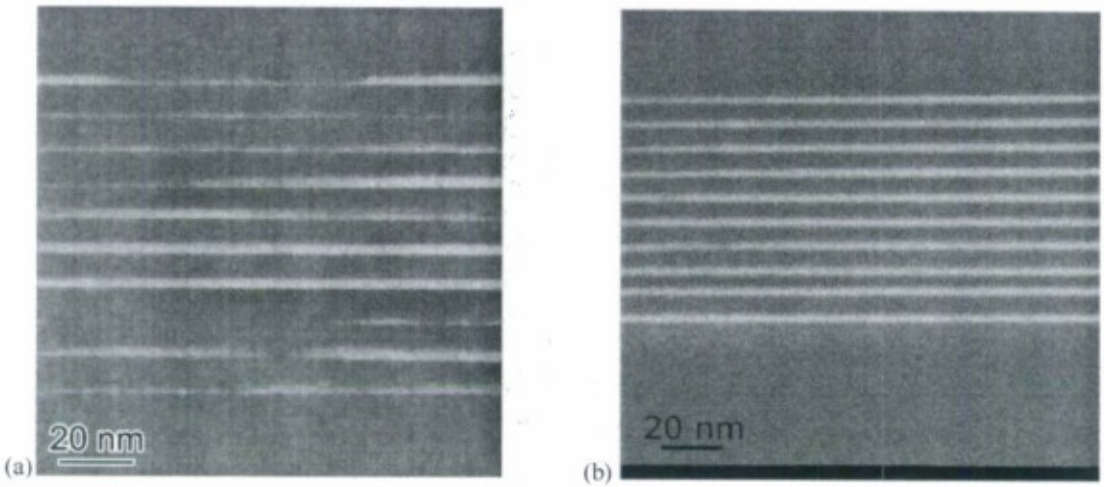

FIG. 5.4. Cross-sectional TEM of 10x MQW solar cell with QW capping layer thickness of (a) 2 nm and (b) 4 nm.

Additional structural characterization was performed by transmission electron microscopy (TEM) to explore the effects of the capping layer thickness on the structure of the InGaN QWs. Figure 5.4 shows cross-sectional TEM images of two 10x InGaN/GaN QW solar cells with different cap layer thicknesses. It is clear in the case of a 2 nm cap layer (see Fig. 5.4(a)) that the QWs (lighter regions) are not of uniform thickness are in places are completely missing. This is an indication that InGaN is desorbing from the well, likely during the barrier growth due to the higher temperatures and presence of hydrogen which tends to etch InGaN. Figure 5.4(b) shows a TEM of a structure with a 4 nm cap and does not show any evidence of InGaN desorption. The wells are of uniform thickness and the interfaces are abrupt. This indicates that the integrity of the InGaN quantum well can be preserved by adequately capping and protecting the well from subsequent growth conditions. This revelation has made it possible to go to high In content wells without loss of structural integrity or reducing indium composition.

Following the establishment of good growth conditions for high indium content QWs, the effect of the number of QWs on device performance was explored. Figure 5.5(a) shows a cross-sectional schematic of the epitaxial structure of a series of devices with a varying number of QWs. The devices were grown by MOCVD on 50 mm double-side-polished sapphire substrates

(a)

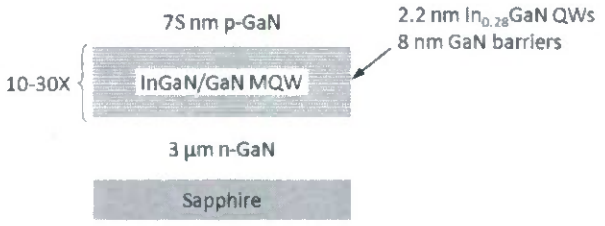

(b)

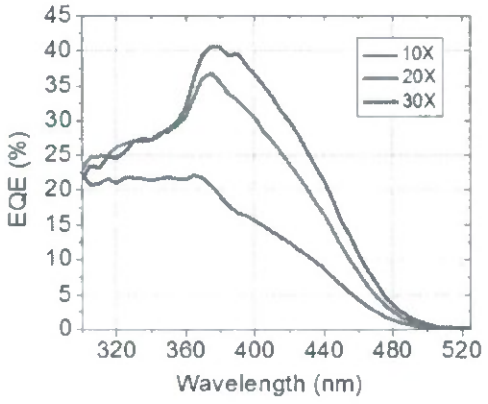

(c)

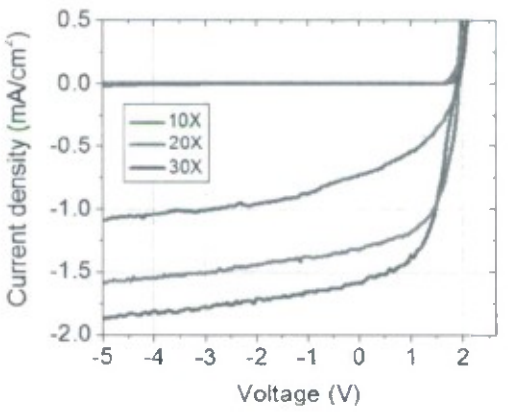

Fig. 5.5. (a) Cross-sectional schematic of the epitaxial structure of a series of devices with a varying number of QWs. (b) Dependence of EQE on wavelength with a varying number of QWs. (c) Dependence of dark and illuminated current density on voltage with a varying number of QWs.

and consisted of a 3 μm n-GaN template, a 10 to 30 period 2.2/8.0 nm $In_{0.28}Ga_{0.72}N$/GaN MQW active region, and a 75 nm p-GaN layer. The final device structure consisted of 1 mm x 1 mm mesas for confining the current flow through the p-GaN, Pd/Au p-contact grids on the top of each mesa with a center-to-center grid spacing of 200 μm, and Al/Au n-contacts around the base of each mesa. As revealed in Figs. 5.5(b) and 5.5(c), the EQE and short-circuit current density both increased with an increasing number of QWs, suggesting that increasing the number of QWs was not inhibiting efficient carrier collection. In addition, for reasons that are still under active investigation, the fill factor also appeared to improve with an increasing number of QWs.

6. Impact of Surface Roughness on the Performance of InGaN-based Solar Cells

Surface roughening is used extensively in the Si solar cell industry to increase device efficiency by scattering the incident light and increasing the optical path length through the absorbing regions of the structure. Previously we presented preliminary results showing the effect of surface roughness on the performance of InGaN-based solar cells. In this section, we attempt to quantify the effect of surface roughness on the optical path length and EQE of InGaN-based solar cells.

A solar cell structure was grown by MOCVD on a 50 mm *c*-plane sapphire substrate. The structure of the solar cell consisted of a 4 μm Si-doped n-GaN template layer, a 60 nm undoped InGaN active region, and a 300 nm Mg-doped p-GaN layer. Hexagonal pits nucleated at the termination of each threading dislocation due to the low growth temperature and the

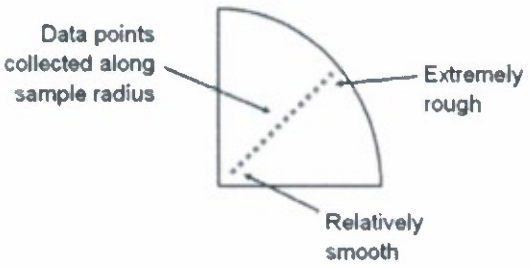

Fig. 6.1. Schematic of the sample layout.

relatively high growth rate of the p-GaN layer. The surface roughness of the p-GaN layer varied from relatively smooth at the center of the sample to very rough at the edge of the sample due to an unintentional gradient in surface temperature. After the device growth was completed the 50 mm sapphire substrate was cleaved into four quarters and one of the quarters was processed into solar cells. The final solar cells consisted of 1 mm x 1 mm mesas for confining the current flow through the p-GaN, Pd/Au p-contact grids on the top of each mesa with a center-to-center grid spacing of 200 μm, and Al/Au n-contacts around the perimeter of each mesa. Following the device processing, the sample was inspected by optical microscopy and AFM and the individual devices were tested by on-wafer probing. As depicted in Fig. 6.1, measurements were collected at several points along the radius of the sample in an attempt to correlate solar cell performance with surface roughness.

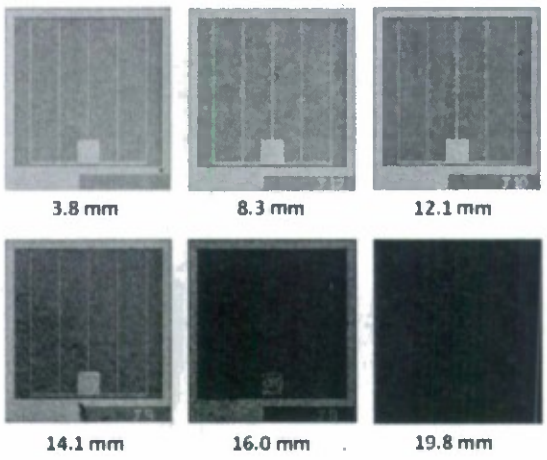

Fig. 6.2. Optical micrographs at various points along the radius of the sample.

Figure 6.2 shows optical micrographs of completed solar cells at various points along the radius of the sample. As illustrated in the micrographs, the intensity of the reflected light decreased from the center to the edge of wafer, indicating that the light was getting scattered more by the rougher surfaces. This increase in scattered light increased the average optical path

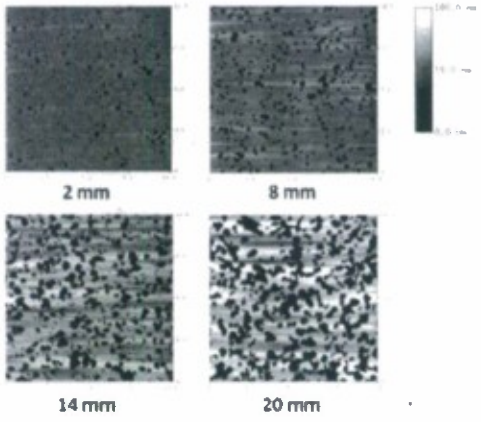

Fig. 6.3. AFM images at various points along the radius of the sample.

length of light through the absorbing regions of the sample and increased the total absorption and EQE of the devices, as discussed below.

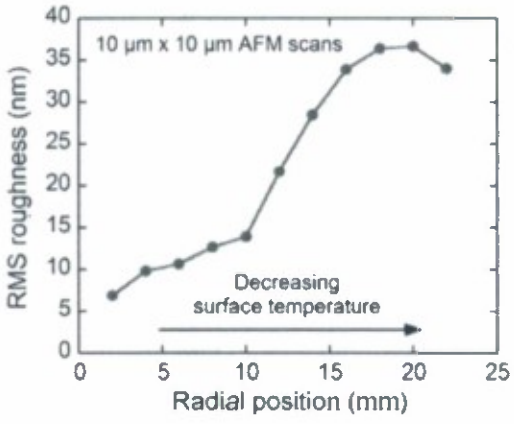

Fig. 6.4. Variation of RMS roughness with radial position.

As discussed above, hexagonal pits nucleated at the termination of each threading dislocation due to the low growth temperature and the relatively high growth rate of the p-GaN layer. Since the surface temperature decreased from the center to the edge of the wafer, the width and depth of the pits increased from the center to the edge of the wafer. This is depicted in Fig. 6.3, which shows AFM images from various points along the radius of the sample. Both the total surface coverage of the pits and RMS roughness increased from the center to the edge of the wafer. The variation of surface roughness with radial position is shown in Fig. 6.4. For radial positions less than 10 mm, the RMS roughness increased relatively slowly, while for radial positions between 10 and 18 mm, the RMS roughness increased relatively quickly. Finally, for radial positions greater than 20 mm, the RMS decreased slightly.

Figure 6.5 shows the variation of the spectral response with radial position. As illustrated by the spectra, there was a significant increase in the peak EQE from the center to the edge of the wafer. In addition, there was a monotonic increase in indium content and the absorption edge going from the center to the edge of the sample. The variation of peak EQE with radial position (Fig. 6.6) showed a similar trend to the variation of RMS roughness with radial position. Moreover, the peak EQE increased from 58.9% from the center of the wafer to 77.5% at the edge of the wafer, representing a fractional increase of 32%. Likewise, the short-circuit current density increased from the center to the edge of the wafer, as depicted in Fig. 6.7. However, unlike the peak EQE, the short-circuit current density did not decrease at the edge of the

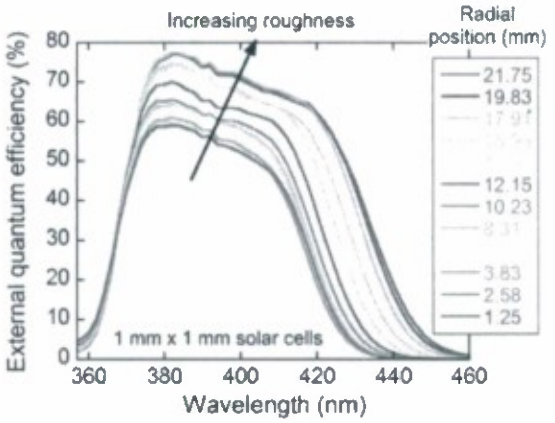

Fig. 6.5. Variation of spectral response with radial position.

wafer, but rather increased monotonically from the center to the edge of the wafer. This occurred because, although the peak EQE decreased slightly at the edge of the wafer, the absorption edge continued to increase all the way to the edge of the wafer, resulting in an increase in the short-circuit current density. Furthermore, the short-circuit current density increased from 1.2 to 2.1 mA/cm^2 from the center to the edge of the wafer, corresponding to a fractional increase of 75%. As expected, the fractional increase of the short-circuit current density was greater than the fractional increase of the peak EQE because the indium content and

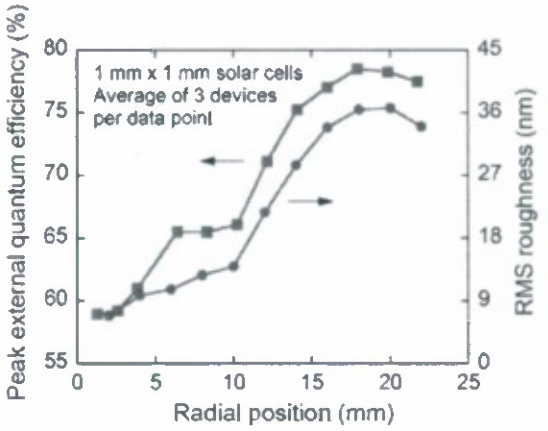

Fig. 6.6. Variation of peak EQE with radial position.

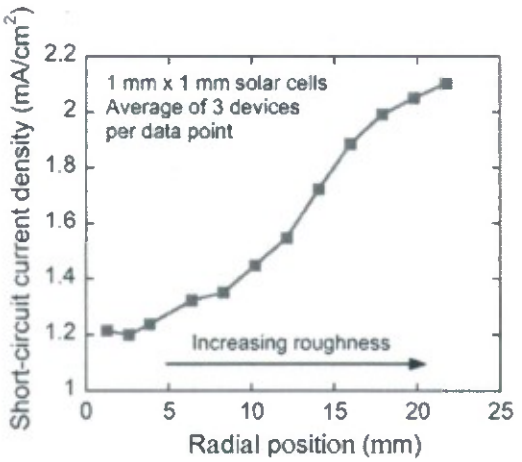

Fig. 6.7. Variation of short-circuit current density with radial position.

the absorption edge increased from the center to the edge of the wafer.

Any time an absorbing layer can be associated with an absorption coefficient and a total absorption in a particular device structure, an equivalent optical path length can be calculated. This equivalent optical path length is typically defined as

$$1 - A \equiv e^{-\alpha L_{eq}} \tag{I}$$

where A is the total absorption, α is the absorption coefficient, and L_{eq} is the equivalent optical path length. If we assume that the internal quantum efficiency (IQE) is uniform across the sample and close to 100% (as shown in the last progress report), then, by definition, the total absorption should be equal to the EQE. Furthermore, if we assume that the absorption coefficient is uniform across the sample, the ratio of the equivalent optical lengths can be calculated for different points on the wafer. Figure 6.8 shows the dependence of the relative optical path length on radial position, where the optical path length at the center of the wafer is used as the reference. As depicted in Fig. 6.8, the optical path length increases by approximately 75% with increasing roughness of the p-GaN layer. This increase should be even larger if the surface is roughened even more and/or if backside mirrors are integrated into the device design. These results demonstrate the applicability of surface roughening to creating high efficiency InGaN-based solar cells.

$$1 - A \equiv e^{-\alpha L_{eq}}$$

$$\ln(1 - A) = -\alpha L_{eq}$$

$$\frac{\ln(1 - A_2)}{\ln(1 - A_1)} = \frac{-\alpha_2 L_{2_{eq}}}{-\alpha_1 L_{1_{eq}}} \approx \frac{L_{2_{eq}}}{L_{1_{eq}}}$$

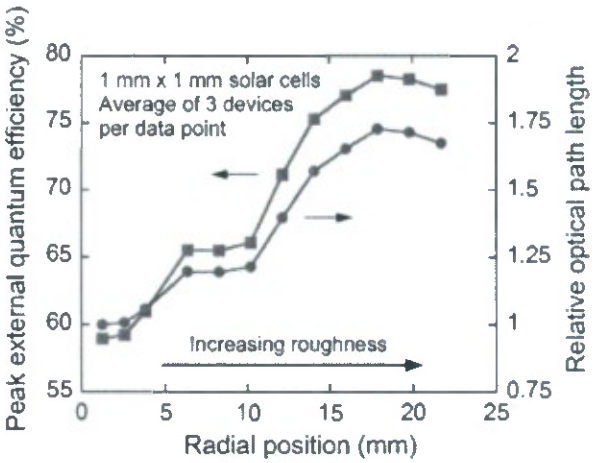

Fig. 6.8. Relative increase in optical path length with radial position.

7. Application of Surface Roughness and Ag Backside Mirrors to High Indium Content Solar Cells

Surface roughening is used extensively by the Si solar cell industry to increase device efficiency by scattering the incident light and increasing the optical path length through the absorbing regions of the structure. Previously we demonstrated the beneficial effects of surface roughening on the performance of low indium content InGaN-based solar cells. Similar benefits can be expected for high indium content InGaN-based solar cells. Figure 7.1(a) shows a cross-sectional schematic of the epitaxial structure of a device with intentionally roughened p-GaN. The device was grown by MOCVD on 50 mm double-side-polished sapphire substrates and consisted of a 3 μm n-GaN template, a 30 period 2.2/8.0 nm $In_{0.28}Ga_{0.72}N$/GaN MQW active region, 75 nm of smooth p-GaN, and 150 nm of intentionally roughened p-GaN. The final device structure consisted of 1 mm x 1 mm mesas for confining the current flow through the p-

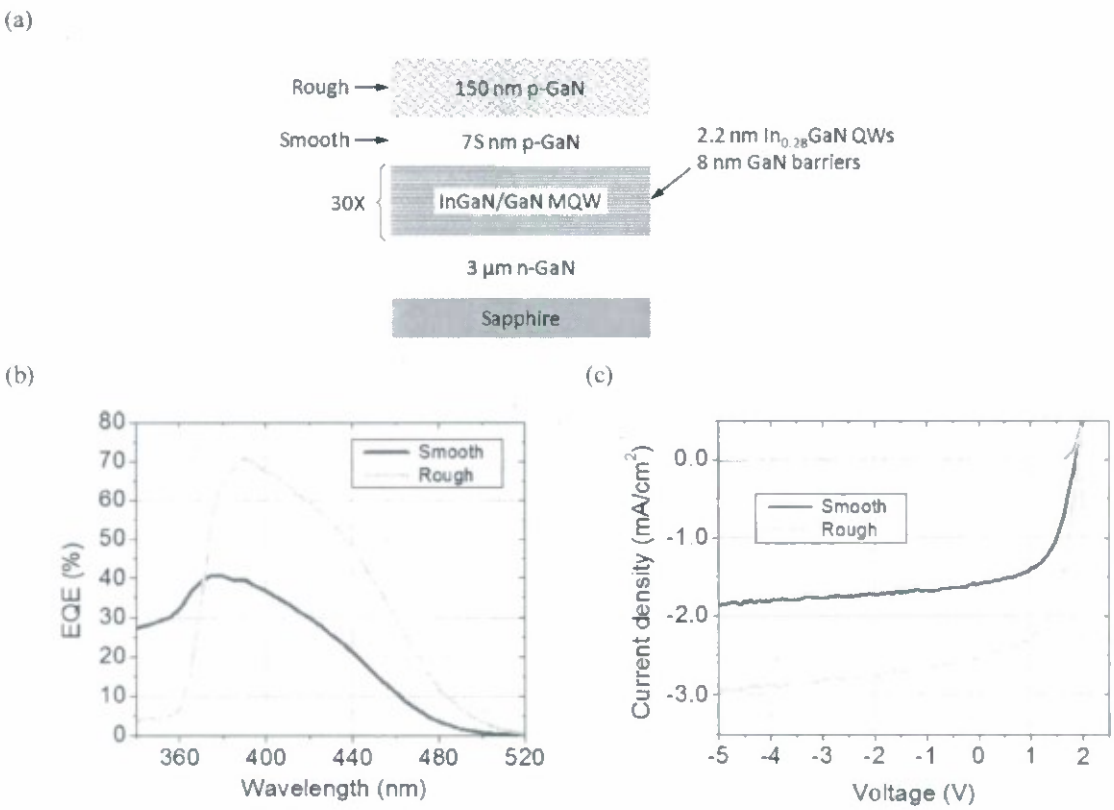

Fig. 7.1. (a) Cross-sectional schematic of the epitaxial structure of a device with intentionally roughened p-GaN. (b) Effect of intentional p-GaN roughening on the dependence of EQE on wavelength. (c) Effect of intentional p-GaN roughening on the dependence of dark and illuminated current density on voltage.

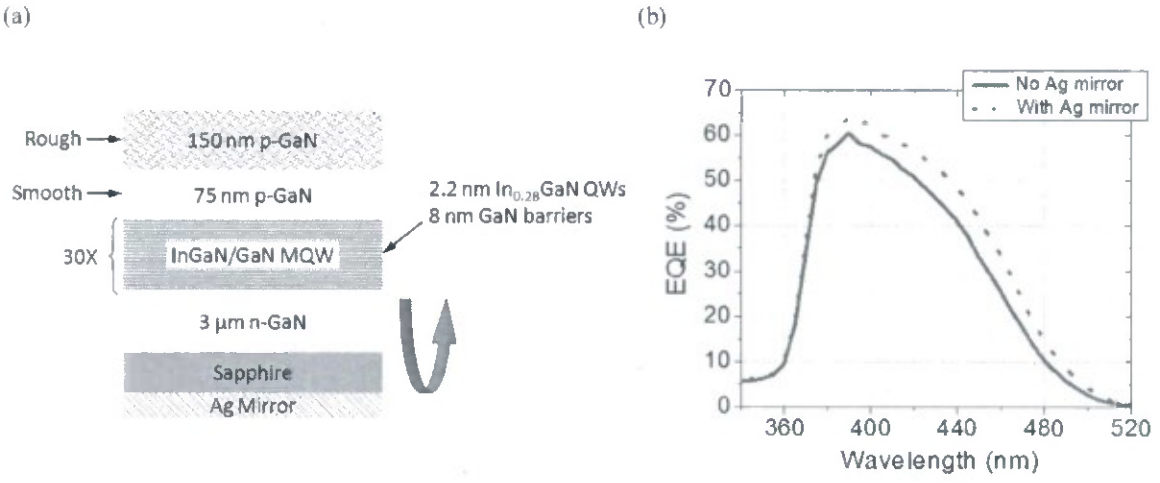

Fig. 7.2. (a) Cross-sectional schematic of the epitaxial structure of a device with intentionally roughened p-GaN and a back side Ag mirror. (b) Effect of a back side Ag mirror on the dependence of EQE on wavelength.

GaN, Pd/Au p-contact grids on the top of each mesa with a center-to-center grid spacing of 200 μm, and Al/Au n-contacts around the base of each mesa. As shown in Figs. 7.1(b) and 7.1(c), intentionally roughening the p-GaN nearly doubled the EQE and increased the short-circuit current density by more than 50%. In addition, roughening the surface did not appear to have any deleterious effects on the open-circuit voltage, the fill factor, or device leakage. Figure 7.2(a) shows a cross-sectional schematic of the epitaxial structure of the same device but with a Ag mirror on the back side of the sapphire substrate. As shown in Fig. 7.2(b), the Ag mirror moderately increased the EQE, especially at longer wavelengths where the absorption on the first pass was relatively low.

8. Thermal Performance of High Indium Content MQW Solar Cells

To determine the performance of InGaN solar cells in concentrator applications the thermal properties must be studied to ensure good performance at high temperatures. In the previous progress report we discussed our preliminary results for temperature measurements on our 30x $In_{0.28}Ga_{0.72}N$/GaN MQW solar cells with 2.2 nm $In_{0.28}Ga_{0.72}N$ wells and 8 nm GaN barriers. A 300 nm thick intentionally roughened p-GaN layer was grown on top of the device to enhance light coupling into the cell as described previously.

Following growth, solar cell devices were fabricated into 1 mm x 1 mm mesas using contact lithography and reactive ion etching. Contacts to the p-GaN layer were formed by depositing a Pd/Au grid with 5 μm wide fingers spaced 200 μm apart and n-type contacts were formed by depositing Al/Au ring around the perimeter of the mesa.

The processed devices were characterized by dark and illuminated *J-V* and power density vs. voltage (P-V) measurements using a Keithley 2635 Picoammeter. Illumination was supplied by an Oriel Xe based solar simulator and AM1.5G filter with illumination intensity of 1 sun as determined by integration of EQE over the AM1.5G spectrum. In order to assess the thermal performance, *J-V* and EQE characteristics were measured on-wafer at temperatures from 22 to 115 °C using a thermoelectric (TE) stage. Additionally, EQE spectra was collected using a Xe broad-band light source coupled with an Oriel 260 monochromator and calibrated with a reference Si photodetector at each stage temperature.

The illuminated *J-V* characteristics at each temperature are shown in Fig. 8.1(a). The device exhibited a fill factor of 63%, V_{OC} of 2.04 V, and J_{SC} of 2 mA/cm^2 at room temperature (22 °C). The *J-V* characteristics behaved as expected with increasing temperature: V_{OC} decreased roughly linearly with increasing temperature as predicted by theory, and J_{SC} increases with temperature. Solar cell output power vs. voltage at each temperature (see Fig. 8.1(b)) show the peak power (P_M) shift toward lower voltage which is consistent with reduced V_{OC} but the peak value increases with temperature and does not immediately drop with temperature as is the case with devices in other solar cell materials such as Ge, Si and GaAs.

The EQE spectra measured at room temperature (22 °C) and 115 °C are shown in Fig. 8.2(a). The long wavelength cutoff corresponds to the InGaN band edge, and shifts toward longer wavelengths as expected. The room temperature EQE response at 460 nm was 26% and increased to 33% at 115 °C. The peak room temperature EQE response was 69% at 390 nm at

and did not increase with temperature indicating that carrier escape from the wells is not thermally limited at room temperature. The low response at short wavelengths is primarily due to absorption above the GaN band gap at ~360 nm and subsequent recombination in the neutral p-GaN layer, and shift in short wavelength response is due to the reduction in the GaN bandgap at higher temperatures. While the entire EQE spectrum is shifts towards longer wavelengths and the area under the curves remains mostly constant, but J_{SC} still increases because the EQE response moves to a portion of the solar spectrum with higher photon flux. To confirm the measured increase in J_{SC} was not an artifact of an inaccurate simulated solar spectrum, theoretical values for J_{SC} were calculated by integrating the measured EQE spectrum at each temperature using the following equation

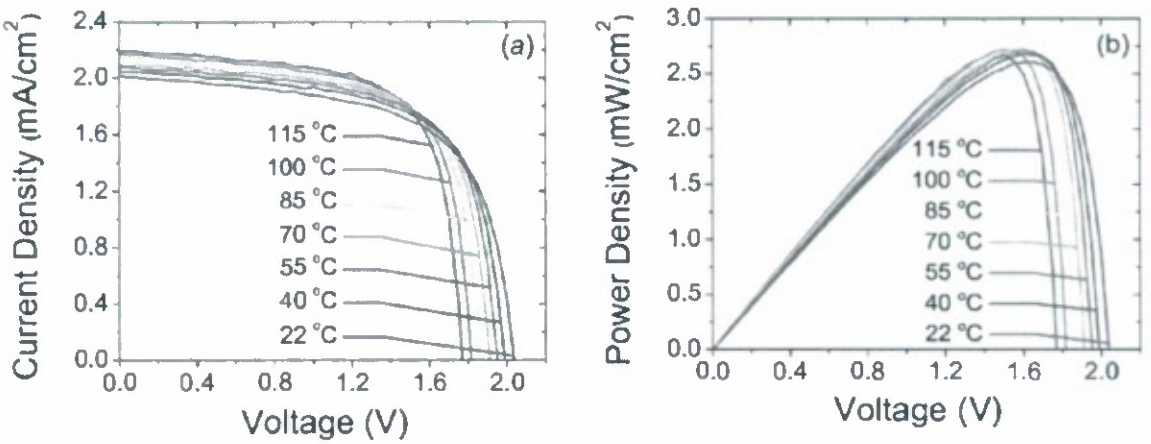

Fig. 8.1. (a) Current density vs. Voltage and (b) output power density vs. voltage at various temperatures for an In0.28Ga0.72N/GaN MQW solar cells.

$$J_{SC,T_n} = q \int_0^\infty EQE_{T_n}(\lambda)\, \Phi(\lambda)\, d\lambda \qquad (3.1)$$

where $J_{SC;Tn}$ is the short circuit current at temperature T_n, $\Phi(\lambda)$ is the AM1.5G photon flux spectra (ASTM G-173-03), and q is the charge of an electron. Both the measured and calculated J_{SC} are plotted vs. temperature in Fig. 8.2(b) and show a high degree of correlation indicating that the simulated solar spectrum is in agreement with the ideal AM1.5G spectrum.

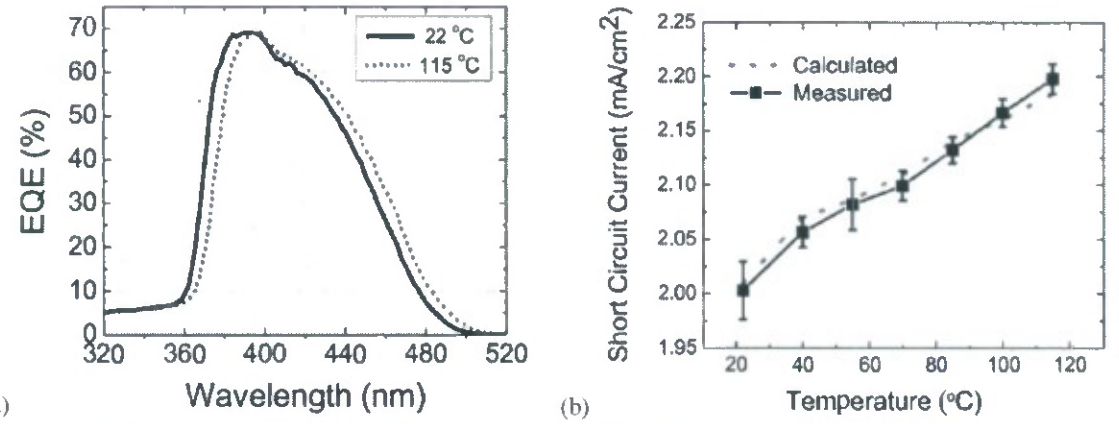

Fig. 8.2. (a) Dependence of EQE on wavelength at room temperature and at 115 °C. (b) Dependence of measured and calculated short-circuit current density on stage temperature.

The peak output power (P_M) increased with increasing temperature to a maximum of 2.72 mW/cm^2 at 70 °C (see Fig. 8.3(e)). Above 70 °C the peak output power saturates and slowly reduces to 2.68 mW/cm^2 at 115 °C. While the peak power does drop at higher temperatures the measured P_M never falls below the room temperature value meaning this device can operate at these temperatures with no loss in efficiency. This behavior is quite different than observed in for other material systems (Ge, Si, GaAs) where peak output power is reduced with an increase in temperature.

The increase in efficiency is not observed for solar devices in other material systems. In order to understand the origin of the origin of the increase in power with temperature and the cause of the roll off in P_M above 70 °C, contributions of the thermal behavior of J_{SC}, V_{OC}, and FF must be considered. The dependence of J_{SC} and V_{OC} on temperature can be seen in Fig. 8.3(a) and (b) respectively. These plots show a linear dependence of J_{SC} and V_{OC} on temperature with thermal coefficients of 0.097 and -0.138 %/K respectively. Here the thermal coefficient (C_x) for parameter x is defined as:

$$C_x = \frac{1}{X_o}\frac{\partial x}{\partial T} \tag{3.2}$$

where x is the parameter (V_{OC}, J_{SC}, FF, P_M), and X_o is the room temperature value of the parameter in question. The net result is that V_{OC} is decreasing faster than J_{SC} is increasing and would not account for the positive coefficient of P_M. Also, since both $C_{V_{OC}}$ and $C_{J_{SC}}$ are relatively

constant with temperature it would not explain the change in C_{P_M} above 70 °C since both coefficients are constant. The dependence of FF on temperature in Fig. 8.3 (c) shows a steep increase in FF with temperature up to 70 °C and a reduced slope at higher temperatures. The thermal coefficient for FF (C_{FF}) is 0.14 %/K from 22 to 70 °C and 0.038 %/K above 70 °C. The calculated coefficients of P_M, found by adding $C_{V_{OC}}$, $C_{J_{SC}}$, and C_{FF} were 0.099 %/K up to 70 °C and -0.003 %/K above 70 °C compare closely to the measured values for C_{P_M} of 0.097 and -.034 %/K for the two temperature ranges respectively. The reduction in C_{FF} at high temperature accounts for the change in C_{P_M} from positive to negative.

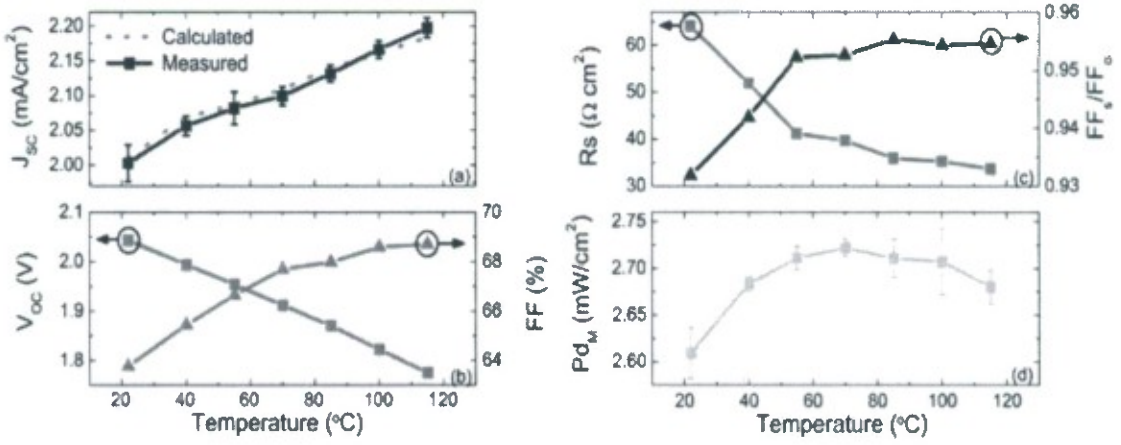

FIG. 8.3. (a) Measured and calculated JSC, (b) VOC, (c) series resistance (Rs), (d) FF and normalized contribution of series resistance (FFS/FFo), and (e) peak output power vs temperature.

The origin of the abrupt change in FF can be approached by analyzing the change in series resistance (R_S) with increasing temperature. Figure 8.3(d) shows the extracted series resistance at each temperature as found by fitting the slope of the illuminated JV curve around V_{OC}. Note the significant reduction in R_S up to 70 °C and the more moderate reduction at higher temperatures. The relationship between fill factor and series resistance can be expressed as:

$$FF_S = FF_o(1 - r_s) \tag{3.3}$$

where FF_o is the ideal fill factor with negligible series resistance and shunt conductance, and r_s is the characteristic series resistance (R_S*J_{SC}/V_{OC}). To isolate the contribution of series resistance, FF_S/FF_o is plotted along with R_S in Fig 8.3(c). It is clear from this plot that the shape of the FF curve is due predominantly to the reduction in *Rs* with increasing temperature. This trend is

likely due to two factors: increased conductivity of p-GaN with temperature for moderate temperatures and reduction of p-contact resistance with temperature, both of which are well documented in the literature.

These results indicate that these devices can operate at elevated temperatures without any degradation in output power. This indicates that InGaN solar cells may be well suited for concentrator applications where significant heating will occur due to the high solar flux.

9. Integration of InGaN-Based Solar Cells with Multijunction GaAs-Based Solar Cells

In this section we discuss how to best integrate InGaN-based solar cells with GaAs-based multijunction solar cells. Figures 9.1(a) and 9.1(b) show the modeled conversion efficiencies of two hybrid solar cell designs with an illumination of 1000 suns under the AM1.5D spectrum at 300K. The model assumes that none of the incident photons are lost to reflection and that every absorbed photon creates carriers that are collected at the terminals of the device. The model also accounts for any necessary optical thinning of a junction to satisfy current-matching requirements for series-connected junctions. In both designs it is assumed that the overlying one junction (1J) InGaN-based cell is electrically isolated from the underlying three junction (3J) or four junction (4J) GaAs-based subcells, which are electrically connected in series. Despite the high potential open circuit voltage and power density for the top 1J InGaN-based cell, the current density of the top cell will nevertheless be significantly lower than the underlying 3J or 4J GaAs-based cells, making current matching unfeasible and necessitating a three- or four-terminal configuration, as discussed in more detail below.

Figure 9.1(a) shows the modeled conversion efficiency of a hybrid 1J + 3J solar cell with an idealized underlying 3J GaAs-based cell and an overlying 1J InGaN-based cell. As depicted in Fig. 9.1(a), the peak modeled efficiency of 58.3% occurs around a band gap of ~2.2 eV for the overlying 1J InGaN-based cell and a band gap of ~1.54 eV for the top junction of the underlying 3J GaAs-based cell, both of which would be technologically challenging to achieve in real-world devices. First, assuming a bowing parameter of 1.4 eV for alloys of InGaN, a band gap of ~2.2 eV for the 1J InGaN-based cell would require an InN mole fraction of ~0.33. This corresponds to a lattice mismatch of ~3.6% with GaN, which is beyond the current technological limits for growing high quality InGaN layers on a GaN template. Second, realizing a band gap of ~1.54 eV for the top junction of the underlying 3J GaAs-based cell would require a lattice-matched quaternary GaInAsP junction, which is a relatively untested technology and may take considerable development.

A more technologically feasible solution is indicated by the vertical red dotted line at 1.83 eV for the top junction of the underlying 3J GaAs-based cell, corresponding to $Ga_{0.51}In_{0.49}P$ lattice-matched to GaAs, which is the standard material used in the top cell of high-efficiency lattice-matched multijunction solar cells. Although larger band gaps can be realized with lattice-matched materials like AlGaAs and AlInGaP, Al-containing materials typically have short

(a) (b)

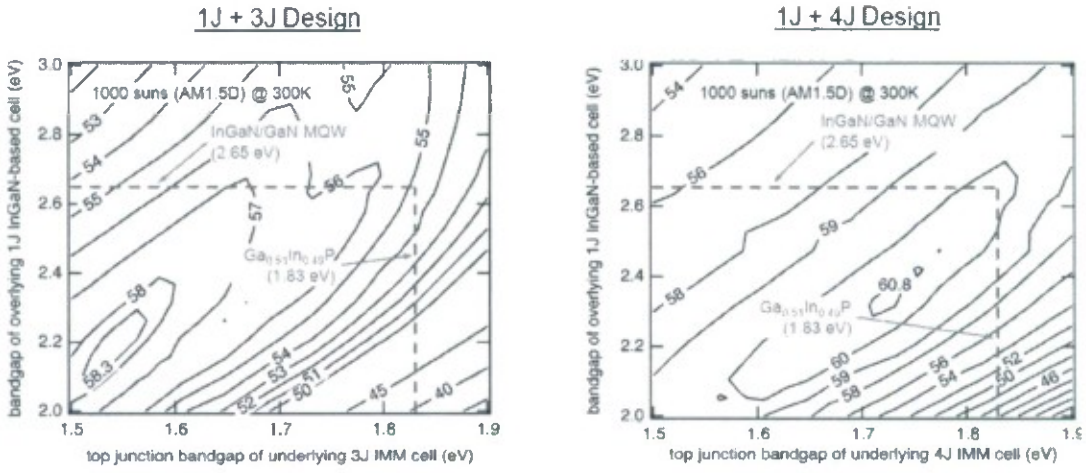

Fig. 9.1. (a) Modeled conversion efficiency for an idealized underlying 3J GaAs-based cell with an overlying 1J InGaN-based cell. Efficiency is calculated for varying band gap of the overlying 1J InGaN-based cell and varying band gap of the top junction of the underlying 3J GaAs-based cell. (b) Modeled conversion efficiency for an idealized underlying 4J GaAs-based cell with an overlying 1J InGaN-based cell. Efficiency is calculated for varying band gap of the overlying 1J InGaN-based cell and varying band gap of the top junction of the underlying 4J GaAs-based cell.

minority carrier diffusion lengths, most likely related to oxygen impurities associated with the presence of Al-containing alloys. In an optimized 1J + 3J structure with an underlying lattice-matched GaAs-based junction, a top junction made of $Ga_{0.51}In_{0.49}P$ would correspond to a band gap of 2.65 eV for the 1J InGaN-based cell, as indicated by the horizontal red dotted line. This band gap would require an InN mole fraction of ~0.20, which corresponds to a lattice mismatch of ~2.2% and is within the current technological limits for growing high quality InGaN layers on a GaN template. However, as shown by the intersection of the two red dotted lines in Fig. 9.1(a), these band gap combinations correspond to a modeled efficiency of 54.4%, which is well below the peak modeled efficiency of 58.3%. Thus, there is large difference between the potential efficiency of an ideal hybrid 1J + 3J cell design and the potential efficiency of a technologically feasible hybrid 1J + 3J cell design.

As an extension of the 1J + 3J device discussed above, Fig. 9.1(b) shows the modeled efficiency of a hybrid 1J + 4J solar cell with an idealized underlying 4J GaAs-based cell and an overlying 1J InGaN-based cell. As depicted in Fig. 9.1(b), the peak modeled efficiency of 60.8% occurs around a band gap of ~2.35 eV for the overlying 1J InGaN-based cell and a band gap of ~1.73 eV for the top junction of the underlying 4J GaAs-based cell. Although both of these band

(a)

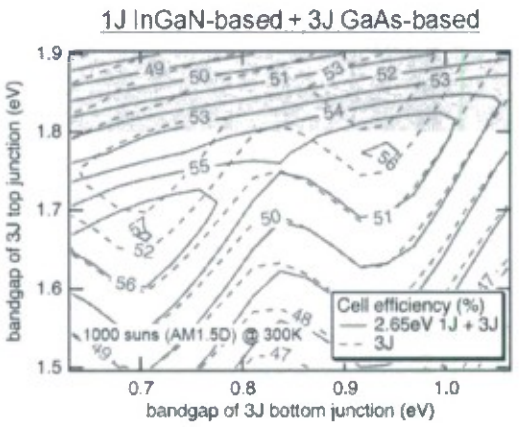

(b)

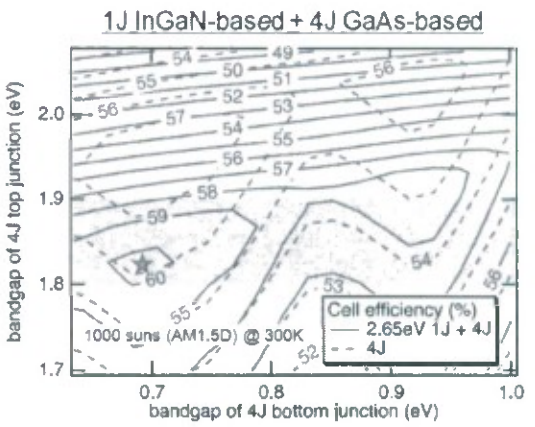

(c)

Configuration	Peak Efficiency* (%)
3J	53.9
1J + 3J	55.5
4J	57.2
1J + 4J	60.3

Fig. 9.2. (a) Modeled conversion efficiency for an idealized underlying 3J GaAs-based cell with an overlying 1J InGaN-based cell. The band gap of the overlying 1J InGaN-based cell is fixed at 2.65 eV and the efficiency is calculated for varying band gaps of the top and bottom junctions of the underlying 3J GaAs-based cell. (b) Modeled conversion efficiency for an idealized underlying 4J GaAs-based cell with an overlying 1J InGaN-based cell. The band gap of the overlying 1J InGaN-based cell is fixed at 2.65 eV and the efficiency is calculated for varying band gaps of the top and bottom junctions of the underlying 4J GaAs-based cell. (c) Table summarized the peak efficiencies of the 3J, 1J + 3J, 4J, and 1J + 4J configurations assuming that the top GaAs-based cell is composed of lattice-matched $Ga_{0.51}In_{0.49}P$ with a band gap of 1.8-1.9 eV (represented by the shaded regions above).

gaps would be technologically challenging to realize in real-world devices, the modeled efficiency of 60.3% at the intersection of the red dotted lines (corresponding to the technologically feasible $Ga_{0.51}In_{0.49}P$ and InGaN band gaps of 1.83 eV and 2.65 eV, respectively) is very close to the peak modeled efficiency of 60.8% discussed above, indicating that there is little difference between the potential efficiency of an ideal hybrid 1J + 4J cell design and the potential efficiency of a technologically feasible hybrid 1J + 4J cell design.

As an extension of the above calculations, Figs. 9.2(a) and 9.2(b) show the modeled conversion efficiencies of hybrid 1J + 3J and 1J + 4J solar cell designs with the band gap of the overlying 1J InGaN-based cell fixed at 2.65 eV. In this case, the efficiency is calculated for varying band gaps of the top and bottom junctions of the underlying 3J or 4J GaAs-based cell. As shown in Fig. 9.2(a), the peak efficiency for the 1J + 3J configuration occurs for a much

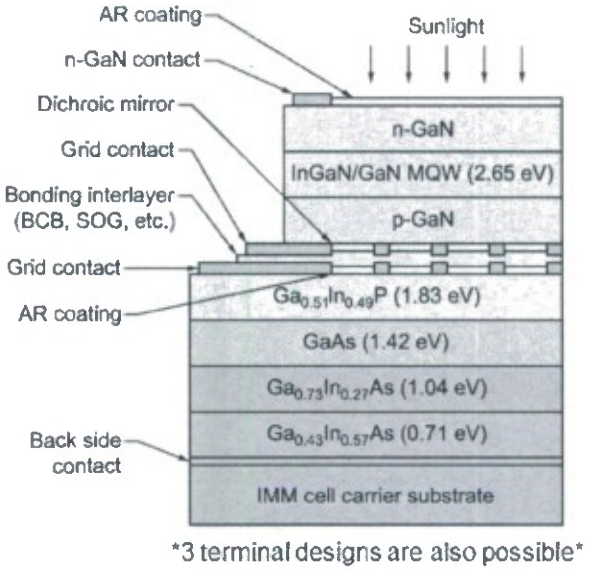

Fig. 9.3. Cross-sectional schematic of the proposed 1J + 4J hybrid bonded cell design.

smaller top junction band gap (~1.67 eV) than the technologically feasible band gap of 1.8-1.9 eV for lattice-matched $Ga_{0.51}In_{0.49}P$ (represented by the shaded region in Figs. 9.2(a) and 9.2(b)). In contrast, as shown in Fig. 9.2(b), the peak efficiency for the 1J + 4J configuration occurs for a top junction band gap of 1.83 eV, which can be easily implemented with a lattice-matched $Ga_{0.51}In_{0.49}P$ junction. The table in Fig. 9.2(c) summarizes the peak efficiencies of the 3J, 1J + 3J, 4J, and 1J + 4J configurations assuming that the top GaAs-based cell is composed of lattice-matched $Ga_{0.51}In_{0.49}P$ with a band gap of 1.8-1.9 eV. As indicated in the table, it should be possible to increase the peak efficiency from 53.9% to 60.3% by moving from a 3J configuration to an optimized 1J + 4J configuration. In addition, as indicated in the table, adding an overlying 1J InGaN-based cell to an underlying 3J GaAs-based cell should only increase the efficiency by ~1.5%, while adding an overlying 1J InGaN-based cell to a underlying 4J GaAs-based cell should increase the efficiency by ~3%. Thus, we conclude that it makes more sense to try to integrate InGaN-based cells with 4J GaAs-based cells than with 3J GaAs-based cells.

The potential advantages of bonding a large band gap InGaN-based top cell to a GaAs-based cell can only be realized with a well-designed, easily executed bonding configuration that minimizes optical losses. Figure 9.3 shows a cross-sectional schematic of the proposed 1J + 4J hybrid cell design. As discussed above, the overlying InGaN-based cell will need to be electrically isolated from the underlying GaAs-based cells because the current density of the

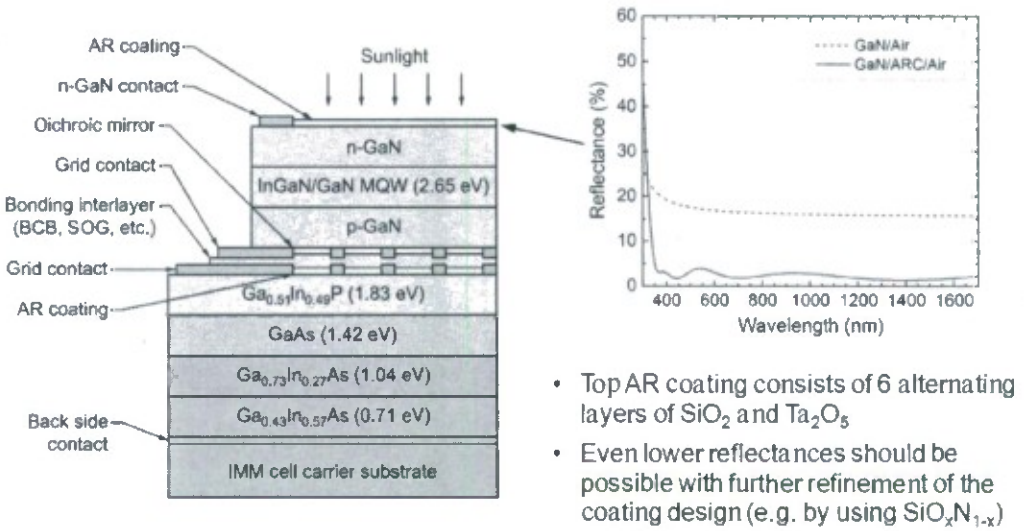

Fig. 9.4. Calculated reflectance spectra at the top GaN/air interface with and without a broadband AR coating.

overlying InGaN-based cell will be significantly lower than the underlying GaAs-based subcells. In addition, a broadband anti-reflection (AR) coating will needed to be used at the top interface of the hybrid cell to minimize reflection at the GaN/air interface, aligned grid contacts will need to be used at the bonding interfaces of both cells to facilitate current spreading and reduce shading loss, and an adhesive low-loss, low-dispersion interlayer, such as benzocyclobutene (BCB) or spin-on-glass (SOG), will need to be used at the bonding interface to electrically isolate the grid contacts and provide good adhesion and mechanical support. Although a four-terminal configuration is shown in Fig. 9.3, it should also be possible to create a three-terminal configuration by shorting together two terminals of the same polarity at the bonding interface. Finally, it will be necessary to have a dichroic mirror (DM) on the top side of the bonding interlayer and an AR coating on the bottom side of the bonding interlayer to reflect high energy photons back to the InGaN-based cell and minimize reflection for lower energy photons, as discussed in more detail below.

Figure 9.4 shows calculated reflectance spectra at the top GaN/air interface with and without a broadband AR coating. The broadband AR coating consists of 6 alternating layers of SiO_2 and Ta_2O_5. As illustrated in Fig. 9.4, the average reflectance between 3.4 eV (the band gap of GaN) and 1.04 eV (the band gap of the first lattice-mismatched GaInAs cell) is reduced from 16.7% without an AR coating to 2.6% with a 6 layer SiO_2/Ta_2O_5 AR coating. Although this

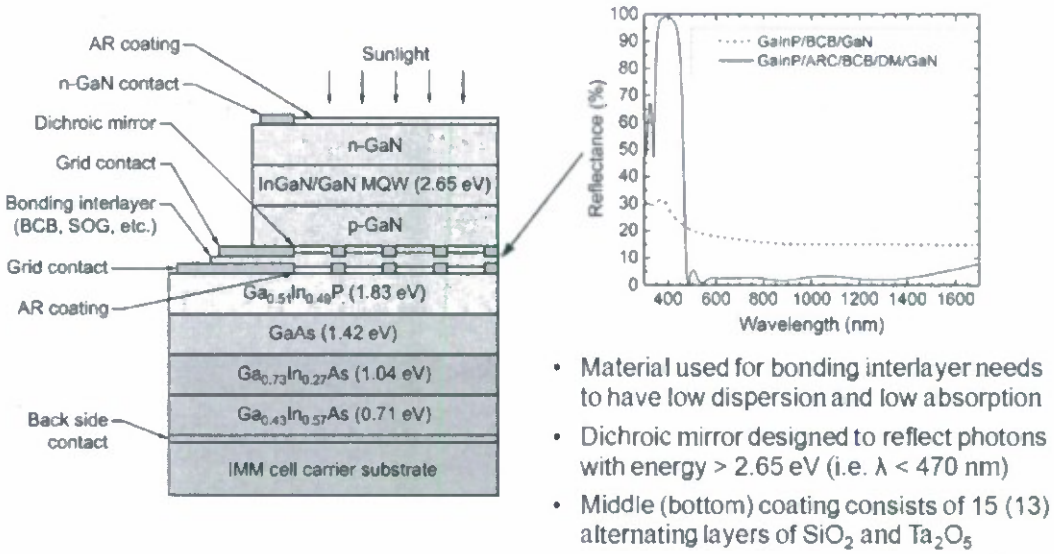

Fig. 9.5. Calculated reflectance spectra at the GaInP/BCB/GaN bonding interface with and without a dichroic mirror.

represents a significant improvement, even lower reflectances should be possible with coatings that utilize materials like SiO_xN_{1-x} with tunable indices of refraction.

The design of the bonding interface is slightly more complicated than the design of the top interface of the cell. As discussed above, the material used for the bonding interlayer needs to have low index dispersion and negligible absorption loss and between 2.65 eV and 0.71 eV. In our initial design, we have chosen to use BCB, which works well as an adhesive material and meets both of these criteria. Second, since there are now three dissimilar materials that need to be optically coupled (GaInP, BCB, and GaN), optical coatings are needed at both the GaInP/BCB interface and the GaN/BCB interface. Third, since the InGaN layers are relatively thin, it would be beneficial if the optical coatings at the bonding interface actually reflected photons with energies greater 2.65 eV for a second pass through the overlying InGaN-based cell. Figure 9.5 shows the calculated reflectivity spectra for the GaInP/BCB/GaN (where the BCB layer is assumed to be 1 μm thick) bonding interface with and without optical coatings. For the case of the GaInP/BCB/GaN bonding interface without any optical coatings, the average reflectance between 2.65 eV and 1.04 eV is 16.3% and the average reflectance between 3.4 eV and 2.65 eV is only 26.6%. For the case of the GaInP/BCB/GaN bonding interface with optical coatings, the average reflectance between 2.65 eV and 1.04 eV is reduced to 2.7% and the average reflectance between 3.4 eV and 2.65 eV is increased to 90.5%. For this design, the

bottom coating consists of 13 alternating layers of SiO_2 and Ta_2O_5 and the top coating consists of 15 alternating layers of SiO_2 and Ta_2O_5.

10. Demonstration of Broadband Optical Coatings on InGaN-based Solar Cells

In this section we demonstrate broadband AR coatings and DMs and apply them to functioning devices. Figure 10.1 shows the measured and calculated reflectance spectra at a GaN/air interface with and without a 6 layer broadband AR coating. The table shows the thickness and composition of each layer of the AR coating. Good agreement is seen between the measured reflectance for a GaN/AR/air interface and the calculated reflectance for a GaN/AR/air interface. As illustrated in Fig. 10.1, the average reflectance between 3.4 eV and 1.04 eV is reduced from 16.6% without an AR coating to 2.8% with a 6 layer SiO_2/Ta_2O_5 AR coating. Although this represents a significant improvement, even lower reflectances should be possible with coatings that utilize materials like SiO_xN_{1-x} with tunable indices of refraction.

Figure 10.2 shows the measured and calculated reflectance spectra at a sapphire/air interface with and without a 14 layer broadband DM. The table shows the thickness and composition of each layer of the DM. Good agreement is seen between the measured reflectance for a sapphire/DM/air interface and the calculated reflectance for a sapphire/DM/air interface.

The DM is designed to be highly reflective for wavelengths less than ~470 nm and anti-reflective for wavelengths greater than ~470 nm. As illustrated in Fig. 10.2, the average reflectance between 2.65 eV (the ideal band gap for the InGaN-based cell) and 1.04 eV is reduced from 7.5% without a DM to 3.5% with a 14 layer SiO_2/Ta_2O_5 DM. Although this

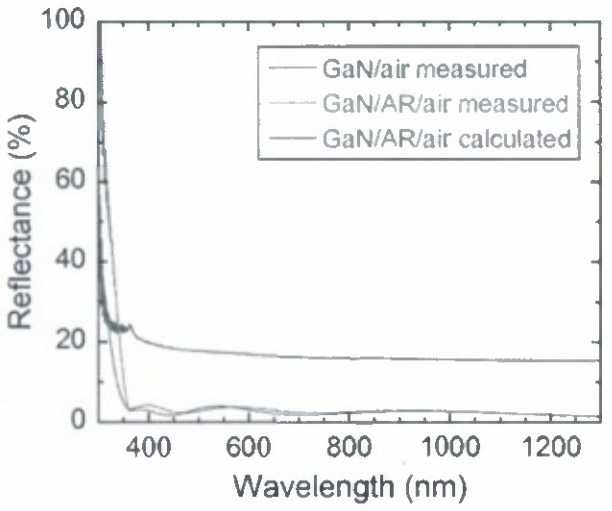

Layer Info	
Material	Width (nm)
Ta_2O_5	73.49
SiO_2	15.78
Ta_2O_5	33.41
SiO_2	41.58
Ta_2O_5	15.55
SiO_2	120.79

Fig. 10.1. Measured and calculated reflectance spectra at a GaN/air interface with and without a 6 layer broadband AR coating. The table shows the thickness and composition of each layer of the AR coating.

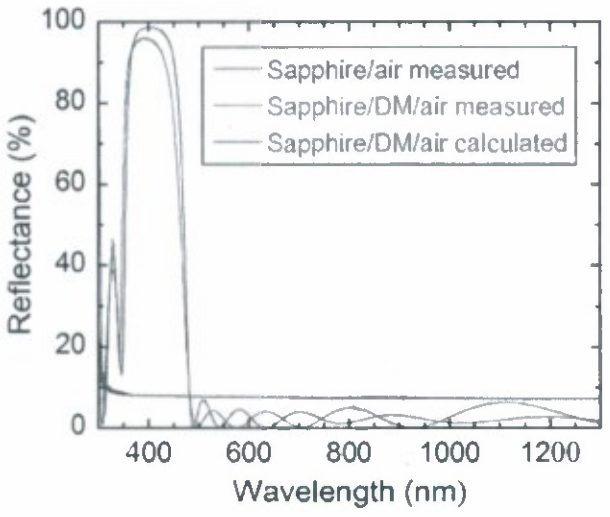

Layer info	
Material	Width (nm)
Ta_2O_5	36.35
SiO_2	19.31
Ta_2O_5	60.49
SiO_2	56.98
Ta_2O_5	37.31
SiO_2	87.56
Ta_2O_5	35.91
SiO_2	70.26
Ta_2O_5	50.17
SiO_2	50.64
Ta_2O_5	57.98
SiO_2	57.98
Ta_2O_5	34.14
SiO_2	157.13

Fig. 10.2. Measured and calculated reflectance spectra at a sapphire/air interface with and without a 14 layer dichroic mirror. The table shows the thickness and composition of each layer of the dichroic mirror.

represents a significant improvement, even lower reflectances should be possible with coatings that utilize materials like SiO_xN_{1-x} with tunable indices of refraction.

Following the above demonstration of high-quality broadband AR coatings and DMs, an identical broadband AR coating was applied to the top side GaN/air interface and an identical broadband DM was applied to back side sapphire/air interface of a Ga-polar *c*-plane solar cell. The structure of the device, which is depicted in the cross-sectional schematic in Fig. 10.3(a), consisted of a double-side-polished sapphire substrate, a 3 μm Si-doped n-GaN template, a 30 period undoped MQW with 2.2 nm InGaN QWs and 8 nm GaN barriers, and an 80 nm Mg-doped p-GaN layer. Figure 10.3(b) shows the EQE spectra of the same device before and after applying optical coatings and Fig. 10.3(c) shows the ratio of the EQE spectra after applying optical coatings to the EQE spectra before applying optical coatings. As illustrated in Figs. 10.3(b) and 10.3(c), the EQE increased across the entire spectral range of the InGaN QWs and the peak EQE increased by 49% following the application of the optical coatings.

Finally, Fig. 10.4(a) depicts the dependence of illuminated current density on voltage for the same device before and after applying optical coatings and Fig. 10.4(b) depicts the dependence of power density on voltage before and after applying optical coatings. As illustrated in Figs. 10.4(a) and 10.4(b), the short circuit current density increased by 44% and the

(a)

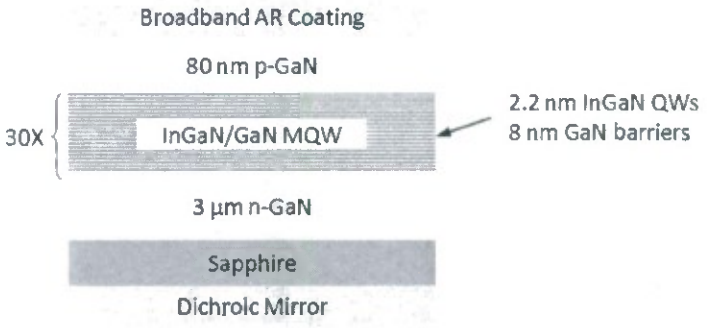

(b)

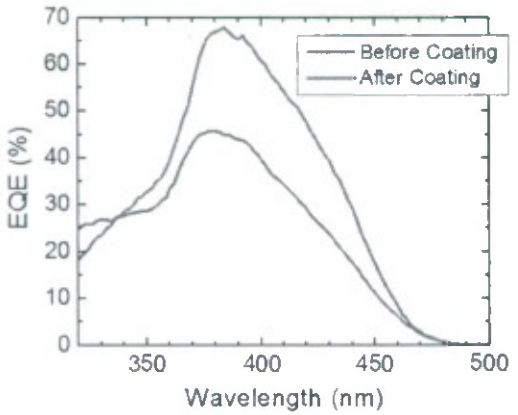

(c)

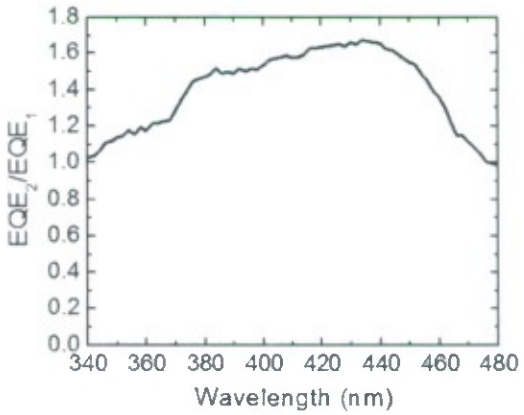

Fig. 10.3. (a) Cross-sectional schematic of the structure of a Ga-polar *c*-plane solar cell with a top side broadband AR coating and a back side dichroic mirror. (b) EQE spectra of the same device before and after applying optical coatings. (c) Ratio of the EQE spectra after applying optical coatings to the EQE spectra before applying optical coatings.

peak power density increased by 43% following the application of the optical coatings. Even though better performance should be possible with coatings that utilize materials like SiO_xN_{1-x} with tunable indices of refraction, these initial results nevertheless indicate that the performance of stand-alone InGaN-based solar cells can be improved significantly with the application of broadband optical coatings. These results also indicate that with the development of broadband optical coatings we are one step closer to successfully integrating InGaN-based solar cells with multijunction GaAs-based solar cells.

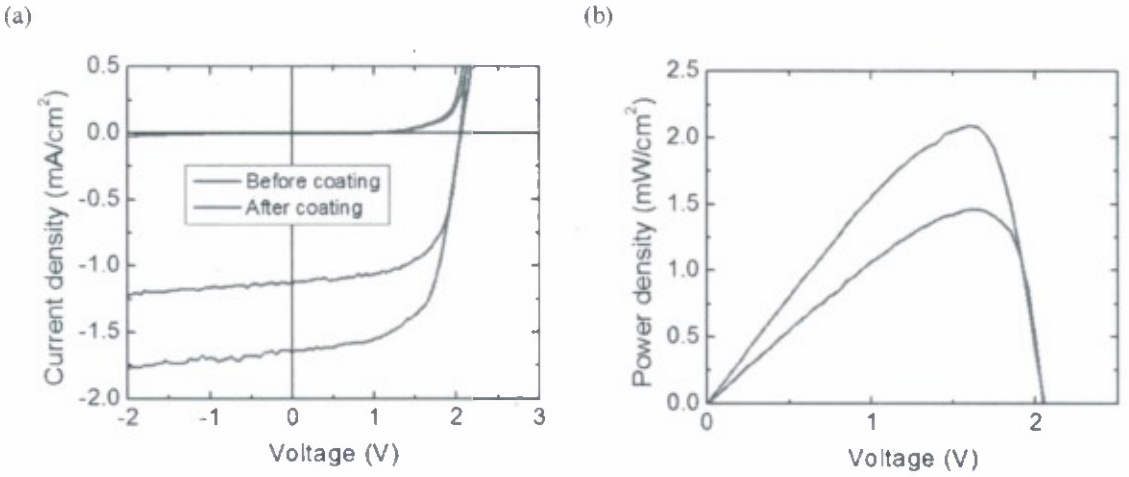

Fig. 10.4. (a) Dependence of illuminated current density on voltage for a Ga-polar *c*-plane solar cell before and after applying optical coatings. (b) Dependence of power density on voltage for the same device before and after applying optical coatings.

11. Ga-polar *c*-plane Solar Cells: Effects of QW Composition on Device Performance

Despite general progress in the performance of Ga-polar *c*-plane InGaN-based solar cells, the performance of devices with higher indium content active regions has been limited by relatively low fill factors and EQE spectra that lack a sharp absorption edge. To investigate these effects systematically, a set of devices was grown with varying quantum well (QW) growth temperature to intentionally vary the indium fraction in the active region. A cross-sectional schematic of the device structure is shown in Fig. 11.1(a) and a summary of QW thickness and composition is shown in Fig. 11.1(b). The width of the QWs ranged from 1.6 to 2.1 nm and the indium fraction in the QWs ranged from 0.06 to 0.28. As depicted in Fig. 11.1(c), the shape

(a)

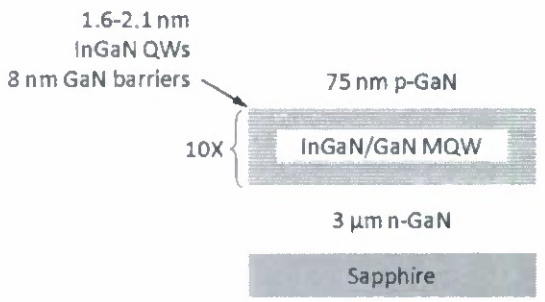

(b)

Run	T_w (C)	L_w (nm)	X_{In}
01AS	765	2.1	0.28
308S	790	1.9	0.22
30AS	815	1.8	0.17
30DS	840	1.7	0.11
30CS	865	1.6	0.06

(c)

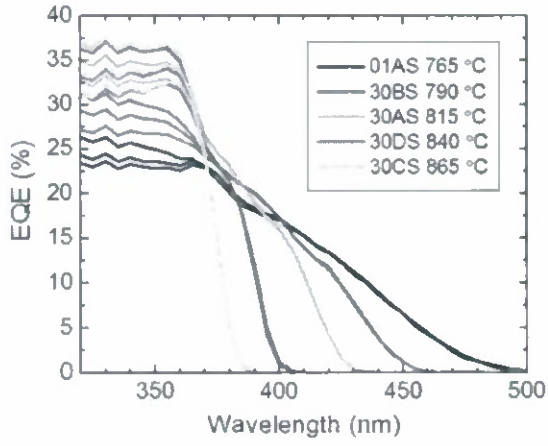

(d)

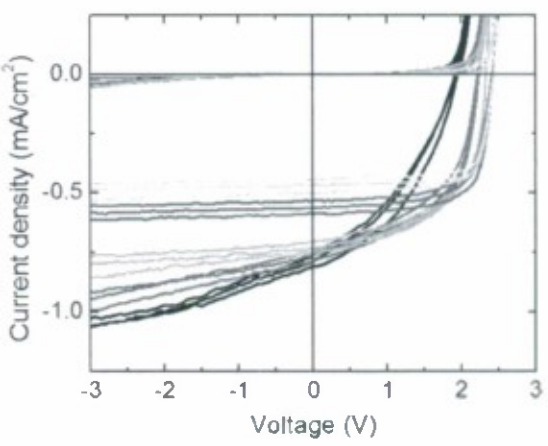

Fig. 11.1. (a) Cross-sectional schematic of the epitaxial structure of a set of Ga-polar *c*-plane solar cells with varying QW growth temperature. (b) Table summarizing QW thickness and composition for the same set of devices. (c) Dependence of EQE on wavelength for the same set of devices. (d) Dependence of dark and illuminated current density on voltage for the same set of devices.

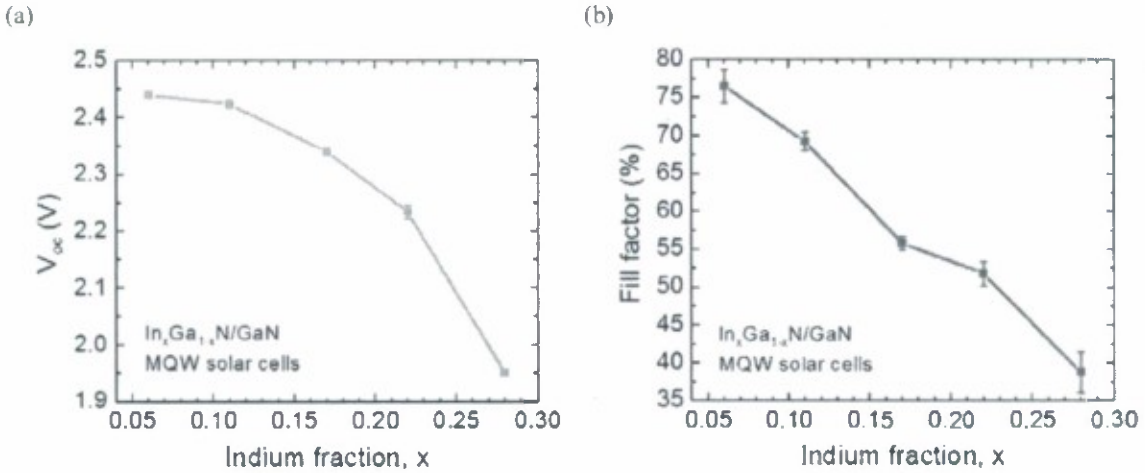

Fig. 11.2. (a) Dependence of V_{oc} on indium fraction for a series of Ga-polar *c*-plane solar cells with varying QW growth temperature. (b) Dependence of FF on indium fraction for the same set of devices.

of the EQE spectra changed significantly with varying indium fraction, becoming less steep and more drawn out with increasing indium fraction. In addition, as depicted in Fig. 11.1(d), the shape of *J-V* curves changed significantly with varying indium fraction, with an increase in the slope of the *J-V* curve around 0 V and a reduction in the sharpness of the knee of the *J-V* curve with increasing indium fraction. These trends are summarized in Figs. 11.2(a) and 11.2(b), which show the dependence of V_{oc} and FF, respectively, on indium fraction. As expected, the V_{oc} decreased with increasing indium fraction and decreasing band gap. However, the FF also decreased precipitously with increasing indium fraction, from an average of 76.5% for devices with $X_{In} = 0.06$ to an average of 38.7% for devices with $X_{In} = 0.28$. To verify that the shapes of the EQE spectra were not influenced by a variation in carrier collection efficiency with wavelength, the EQE spectra and absorption spectra were compared for all devices. As depicted in Fig. 11.3, the devices exhibited good agreement between the shape of the absorption spectra and the shape of the EQE spectra, indicating that the carrier collection efficiency was not wavelength dependent.

The shape of the EQE spectra shown in Fig. 11.1(c) can be explained by the presence of large polarization-related electric fields in the InGaN-based QWs and the effect that they are expected to have on the absorption spectra. The schematic on the left side of Fig. 11.4 shows the effect of an applied electric field on the energy band diagram and the electron and hole wavefunctions of a 15 nm GaAs QW with infinite barriers. The applied electric field tilts the

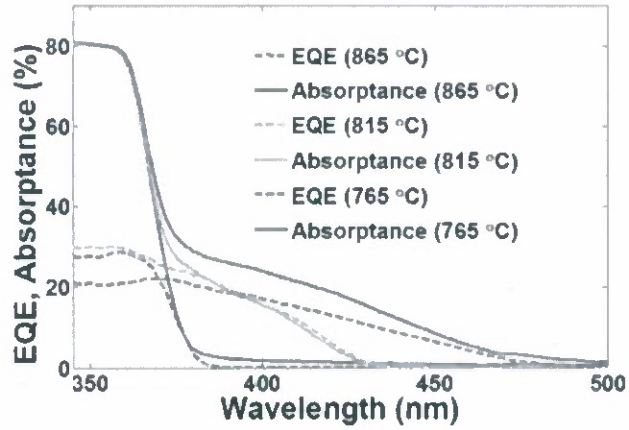

Fig. 11.3. (a) Dependence of EQE and absorptance on wavelength for a series of Ga-polar *c*-plane solar cells with varying QW growth temperature.

conduction band and valence band in the QW, creating a spatial separation between the electron and hole wavefunctions. This increases the overlap of the lowest energy wavefunctions at energies below the zero-field band gap and decreases the overlap of the lowest energy wavefunctions at energies above the zero-field band gap, with the net effect of "smearing" out the absorption edge of the QWs in the presence of an applied electric field, as depicted in the absorption spectra on the right side of Fig. 11.4. Although the absorption spectra shown in Fig. 11.4 are for GaAs QWs with applied electric fields, similar effects should be expected for built-in polarization-related electric fields, as in the case on InGaN QWs. Increasing the indium fraction in the QWs should have the effect of smearing out the absorption spectra, which indeed is what is observed in Figs. 11.2(c) and 11.3.

The change in the shape of the *J-V* curves with varying indium fraction is more difficult to understand. As discussed above, increasing the indium fraction in the QWs increases the slope of the *J-V* curve around 0 V and decreases the sharpness of the knee of the *J-V* curve. This change in the photocurrent with bias could have a number of potential physical origins. These potential physical origins include a change in the absorption spectra with bias, a change in the carrier collection efficiency with bias, and a change in the depletion region width with bias.

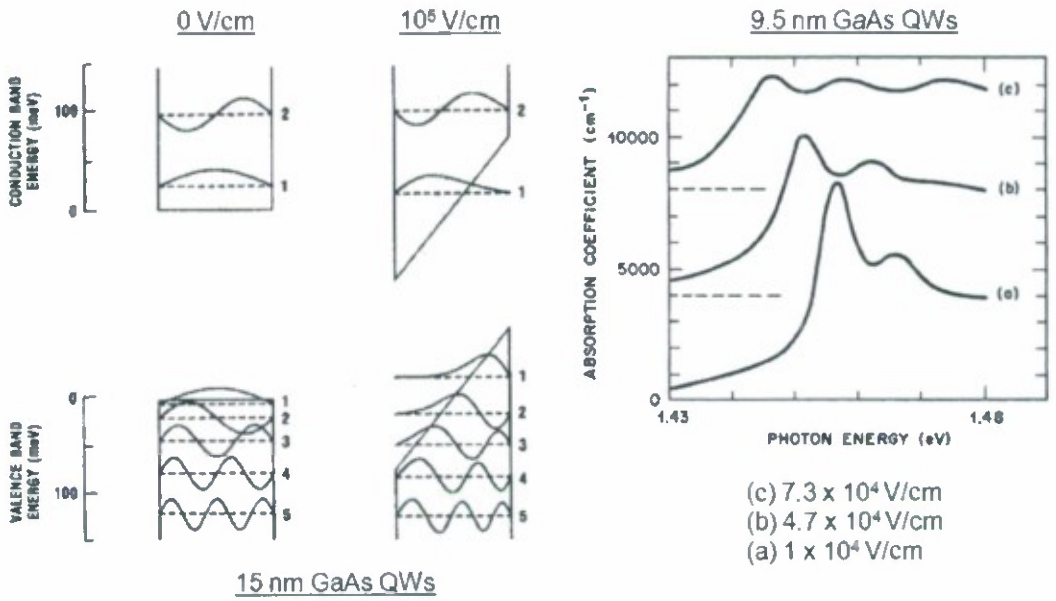

S. Schmittrink, D. S. Chemla, and D. A. B. Miller, Advances in Physics **38**, 89 (1989).
D. A. B. Miller *et al.*, Phys. Rev. B **32**, 1043 (1985).

Fig. 11.4. Schematic showing the effect of an applied electric field on the energy band diagram and the electron and hole wavefunctions of a 15 nm GaAs QW with infinite barriers (left). Dependence of absorption spectra on applied electric field for an AlGaAs/GaAs MQW with 9.5 nm GaAs QWs (right).

Regardless of the physical origin of the above observations, there was a clear correlation between increasing indium fraction in the QWs, low fill factors, and EQE spectra that lack a sharp absorption edge. These results suggested that there may some limitations for Ga-polar *c*-plane solar cells due to the presence of large polarization-related electric fields. They also suggest that there may be some advantages for semipolar or nonpolar solar cells due a reduction or elimination of the polarization-related electric fields in semipolar and nonpolar heterostructures.

12. First Semipolar InGaN-Based Solar Cells

Following the completion of the experiments on the effects of QW composition on device performance, we began to suspect that Ga-polar *c*-plane solar cells were possibly limited by the presence of large polarization-related electric fields. As an alternative to growing Ga-polar *c*-plane InGaN-based solar cells, we started to investigate growing InGaN-based solar cells along other crystallographic orientations with smaller polarization-related electric fields. In this section, we discuss our initial efforts to grow InGaN-based solar cells on free-standing $(20\bar{2}1)$ GaN substrates.

Figure 12.1 shows a cross-sectional schematic of the epitaxial structure of a set of $(20\bar{2}1)$ MQW structures with a varying number of QWs. The structures were grown without any p-GaN layers to investigate the properties of the as-grown MQWs by photoluminescence (PL), fluorescence microscopy (FLM), XRD, and AFM. All structures had a peak PL wavelength of ~460 nm and an indium mole fraction of ~0.20 in the QWs. Figure 12.1(b) shows FLM images for a set of MQW structures with varying

(a)

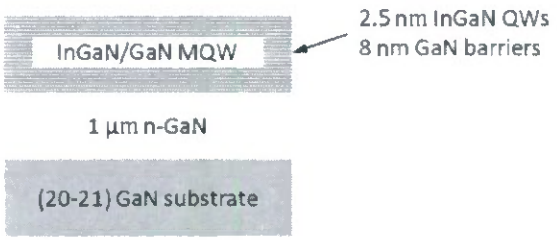

(b)

Fig. 12.1. (a) Cross-sectional schematic of the epitaxial structure of a set of $(20\bar{2}1)$ MQW structures with a varying number of QWs. (b) FLM images of the same set of devices.

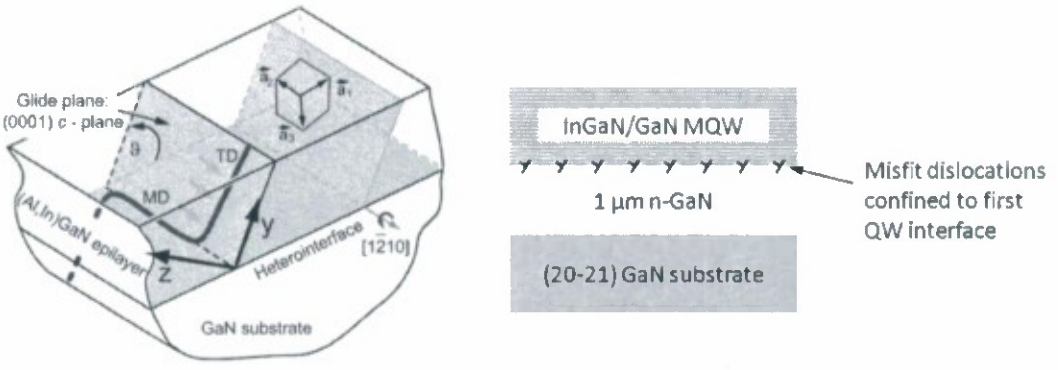

Fig. 12.2. (a) Schematic of MD formation by glide of a preexisting TD for a (20$\bar{2}$1) heterostructure showing the [1$\bar{2}$10] line direction and the Burgers vectors of the MD. (b) Cross-sectional schematic of the epitaxial structure of a (20$\bar{2}$1) MQW structure showing the MDs confined to the first QW interface.

numbers of QWs. The projection of the *c*-axis is towards the top of the page in these images. One-dimensional misfit dislocations (MDs) appear in the FLM images as dark horizontal lines in the <11-20> direction. Although the density of MDs does appear to increase with an increasing number of QWs, the MDs should remain confined at the first QW interface, making it possible to isolate the MDs from the collection of minority carriers. This confinement of the MDs to the first QW interface is depicted in Fig. 12.2. For a short period superlattice such as an InGaN/GaN MQW, the MQW should behave like a single strained InGaN layer, and the MDs should remain confined at the first QW interface, gliding with a [1$\bar{2}$10] line direction along the intersection of the (0001) c-plane and the first InGaN/GaN interface.

In addition to remaining confined at the first QW interface, the MDs do not appear to have a significant effect on the surface morphology of the MQWs. Figure 12.3 shows 12.5 μm x 12.5 μm AFM images and measured RMS roughness values for a (20$\bar{2}$1) GaN template grown at 1180 °C, a (20$\bar{2}$1) GaN template grown at 1180 °C followed by an 8 nm barrier at 780 °C, and a set of (20$\bar{2}$1) MQW structures with a varying number of QWs. The projection of the *c*-axis is towards the upper right corner of the page in these images. Although the 20X and 25X samples with higher densities of MDs appear to have some additional step-like features that are probably related to the MDs, all of the samples are still very smooth, with RMS roughness values ranging from 0.144 to 0.295 nm.

Figures 12.4(a) and 12.4(b) show high-resolution reciprocal space maps (RSMs) measured by XRD for a (20$\bar{2}$1) MQW structure with 25 QWs and for a (20$\bar{2}$1) solar cell structure with 30 QWs and a ~120 nm p-GaN layer, respectively. The superlattice peaks for both

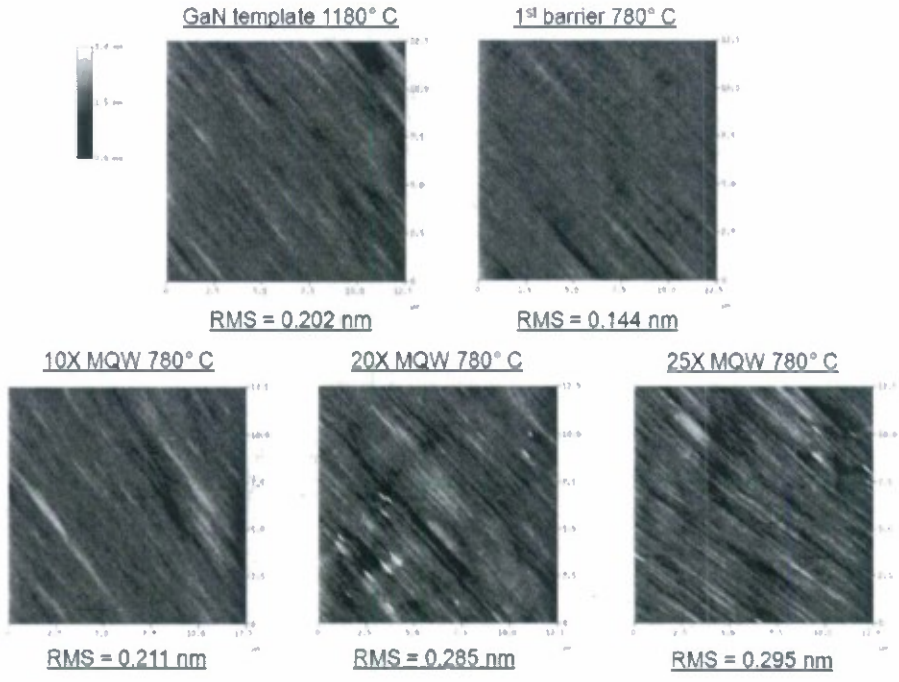

Fig. 12.3. (a) 12.5 μm x 12.5 μm AFM images and measured RMS roughness values for a $(20\bar{2}1)$ GaN template grown at 1180 °C, a $(20\bar{2}1)$ GaN template grown at 1180 °C followed by an 8 nm barrier at 780 °C, and a set of $(20\bar{2}1)$ MQW structures with a varying number of QWs.

RSMs are offset slightly along the Q_x axis from the GaN substrate peak, indicating that the InGaN/GaN MQWs are partially relaxed. However, the superlattice peaks for both RSMs are also relatively sharp and aligned to one another along the Q_x axis, indicating that all layers of the MQW have the same lattice constant and are coherently strained to one another. Moreover, for the solar cell structure shown in Fig. 12.4(b), the p-GaN appears to be coherently strained to the underlying InGaN/GaN MQW because of the presence of an additional GaN peak that is offset from the GaN substrate peak and is aligned with the superlattice peaks along the Q_x axis.

Following the investigation of MQW structures without p-GaN layers, full solar cell structures were grown with ~75 nm of p-GaN on top of the QWs. The structure of these samples is illustrated in the cross-sectional schematic in Fig. 12.5(a). FLM images of devices with varying numbers of QWs are presented in Fig. 12.5(b). The projection of the *c*-axis is towards the top of the page in these images. While the density of the MDs looks similar for all of the devices, this may be limited by the resolution of the FLM images.

Absorptance spectra for all 4 devices are shown in Fig. 12.6. Compared to Ga-polar *c*-plane devices with similar indium fractions in the QWs (see Fig. 11.1(c)), the absorption edge of

(a) (b)

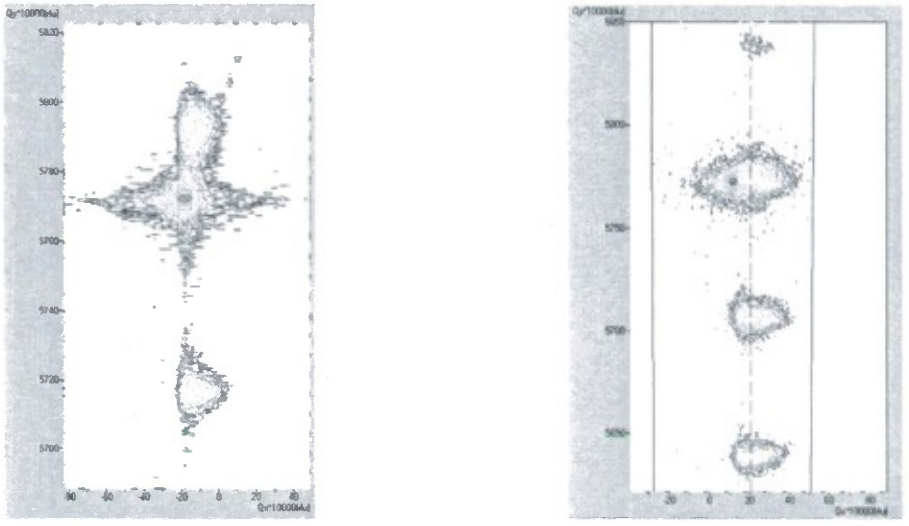

Fig. 12.4. (a) RSM of a $(20\bar{2}1)$ MQW structure with 25 QWs. (b) RSM of a $(20\bar{2}1)$ solar cell structure with 30 QWs.

the $(20\bar{2}1)$ solar cells looks significantly sharper. This improvement in the shape of the absorptance spectra is most likely related to a reduction of the built-in polarization-related electric fields in $(20\bar{2}1)$ QWs compared to *c*-plane QWs.

Figure 12.7 presents data on device performance for the same set of samples. Unfortunately, the EQE spectra appear very similar for all four samples, do not correspond well with the measured absorptance spectra (Fig. 12.6), and show little dependence on the number of QWs, as depicted in Fig. 12.7(a). In addition, although the V_{oc} values are very high (2.15 to 2.29 V) for samples with an absorption edge of ~460 nm, the FF values are very low, ranging from 33.4 to 42.9% and showing no clear dependence on the number of QWs, as depicted in Fig. 12.7(b) and summarized in the table in Fig. 12.7(c).

The similarity of the EQE spectra for devices with different numbers of QWs and relatively wide active regions indicates that the device performance may be limited by unintentional background n-type doping in the active region. Figure 12.8 depicts SIMS measurements showing the concentration profiles for carbon, oxygen, hydrogen, and silicon for a $(20\bar{2}1)$ sample with layers with varying growth conditions. As denoted in the figure, layers 2, 3, and 4 correspond to growth conditions that are similar to the active regions in our devices and

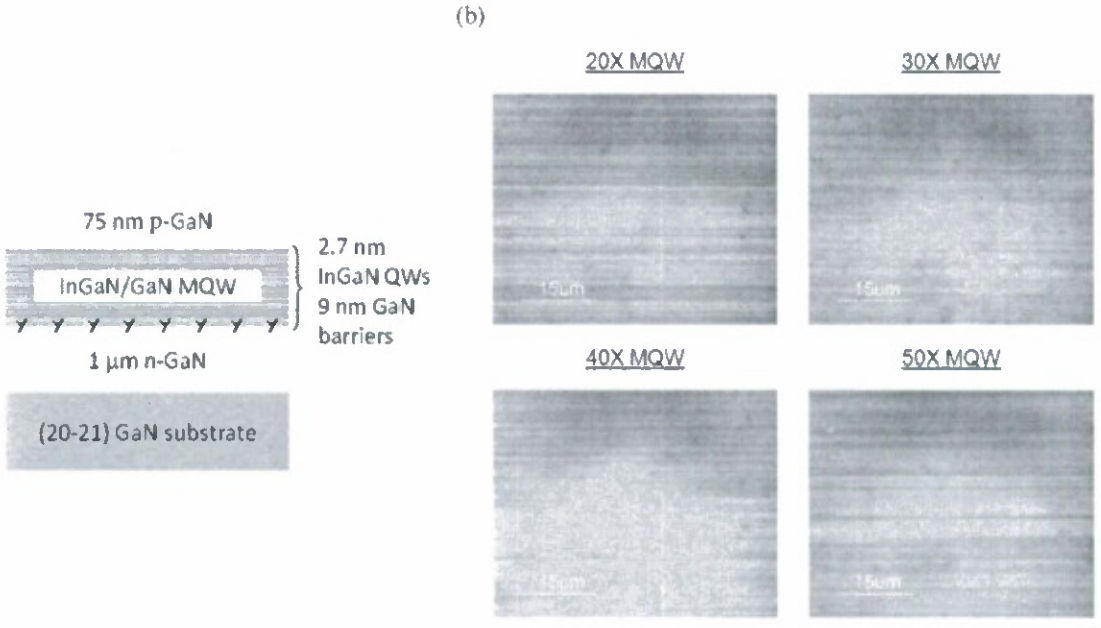

Fig. 12.5. (a) Cross-sectional schematic of the epitaxial structure of a set of $(20\bar{2}1)$ solar cells with a varying number of QWs. (b) FLM images from the same set of devices.

indicate that the oxygen concentration in the active region of our devices is in the range of $\sim 2\times10^{17}$ cm^{-3}. Since oxygen acts as a shallow n-type dopant in GaN, an oxygen level of $\sim 2\times10^{17}$ cm^{-3} should severely limit the thickness of the depletion region in our devices. Figure 12.9 shows the calculated dependence of depletion region width on unintentional background n-type doping in the active region of an InGaN-based solar cell assuming a p-type doping level of $\sim 5\times10^{18}$ cm^{-3}. As indicated in the figure, our current background oxygen level of $\sim 2\times10^{17}$ cm^{-3} corresponds to a depletion region width of ~125 nm, which is less than the thicknesses of the active regions of the devices discussed, which range from ~200 nm for the 20X MQW device to ~500 nm for the 50X MQW device. This suggests that carriers are only being collected from the top 10 to 15 QWs for all four devices and explains why the EQE spectra look so similar for all four devices. This also explains why the photocurrent for all four devices changes so drastically with bias (Fig. 12.7(b)), since the depletion region width and hence the photocurrent should both vary strongly with bias.

There are several possible ways to overcome these issues with unintentional background n-type doping. First, we can try to grow $(20\bar{2}1)$ MQWs with thinner barriers and thicker QWs to decrease the total MQW thickness to be less than the depletion region width due to unintentional background n-type doping. Second, we can try to reduce the oxygen levels in

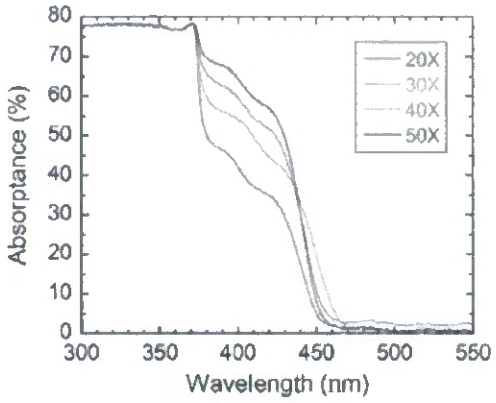

Fig. 12.6. Dependence of absorptance on wavelength for a set of $(20\bar{2}1)$ solar cells with a varying number of QWs.

the $(20\bar{2}1)$ QWs by adjusting the growth conditions. Third, we can try to reduce the oxygen levels in the $(20\bar{2}1)$ QWs by modifying the reactor hardware to reduce sources of oxygen contamination. Finally, we can try growing solar cells on different semipolar orientations, which have been shown previously to have widely varying levels of unintentional oxygen incorporation under identical growth conditions [S. C. Cruz *et al.*, J. Cryst. Growth **311,** 3817 (2009)].

Figure 12.10 summarizes the results of trying to grow solar cells on different semipolar orientations. All samples contained undoped GaN layers that were grown with a TEG flow of 35 sccm and an NH_3 flow of 4 slm, similar to the growth conditions used for semipolar MQWs and corresponding to a growth rate of about 0.12 nm/s. SIMS measurements were performed to measure the dependence of oxygen concentration on temperature for samples grown on different semipolar orientations. As shown in Fig. 12.10, the oxygen concentration of the (20-21) samples ($\sim 5\times10^{16}$ cm^{-3}) was reduced by about a factor of 4 from the measurements on previous samples ($\sim 2\times10^{17}$ cm^{-3}, see Fig. 12.8), most likely due to normal variations in background impurities in the MOCVD reactor. However, the oxygen concentration of the (20-2-1) and (10-1-1) samples ($\sim 2\text{-}3\times10^{16}$ cm^{-3}) was only reduced by about a factor of 2 compared to the (20-21) samples, which shouldn't have a significant effect on the depletion region width because it depends on the square root of impurity concentration. Only the (11-2-2) plane showed a significant decrease in oxygen concentration. However, additional experiments showed that the (11-2-2) plane had very low indium incorporation compare to other typical planes for InGaN growth (data not shown), ruling out the (11-2-2) plane as a potential plane for InGaN-based solar cell growth.

(a)

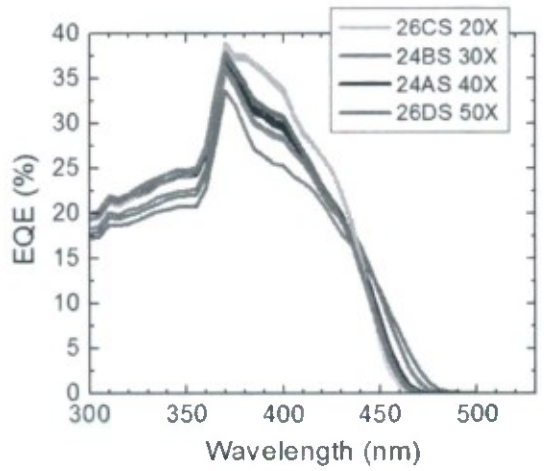

(b)

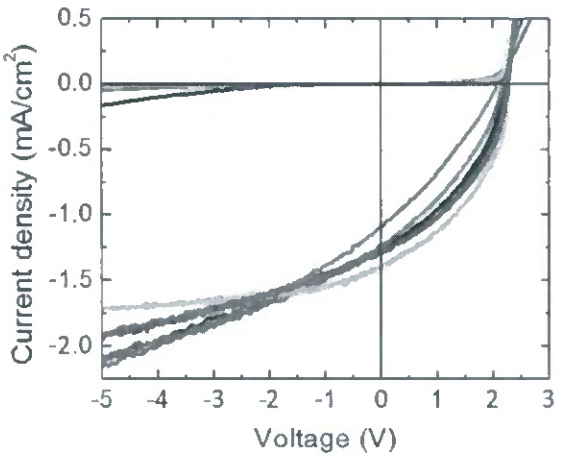

(c)

Run	$N_{w\text{-}tot}$	FF_{avg} (%)	Voc_{avg} (V)
26CS	20	42.9	2.29
24BS	30	33.4	2.15
24AS	40	38.4	2.24
26DS	50	41.0	2.28

FIG. 12.7. (a) Dependence of EQE on wavelength for a set of $(20\bar{2}1)$ solar cells with a varying number of QWs. (b) Dependence of dark and illuminated current density on voltage for the same set of devices. (c) Table summarizing V_{oc} and FF for the same set of devices.

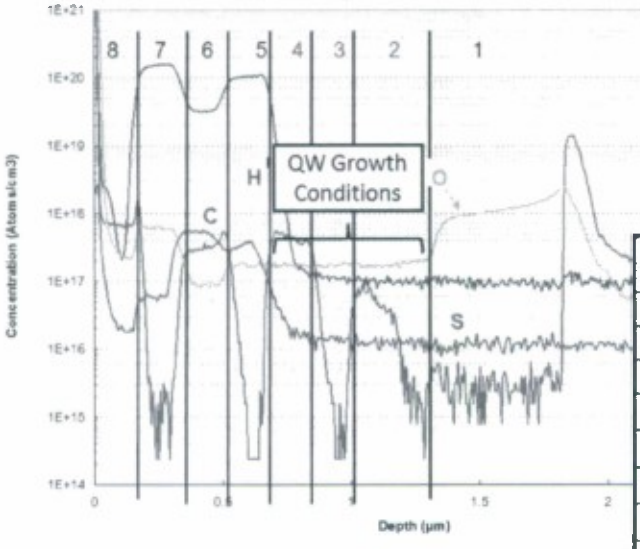

Layer	T(C)	Ga (sccm)	NH_3 (slm)	Mg[2] (sccm)	H_2/N_2
1	1180	TMGa=15	3.2	–	N_2
2	800	TEGa=15	5.5	–	N_2
3	800	15	3.2	–	N_2
4	800	15	2	–	N_2
5	820	35	4	25	H_2
6	780	35	4	10	H_2
7	880	35	4	35	H_2
8	880	35	5.5	–	H_2/N_2

FIG. 12.8. SIMS measurements showing the concentration profiles for carbon, oxygen, hydrogen, and silicon for a $(20\bar{2}1)$ sample with layers grown under varying conditions.

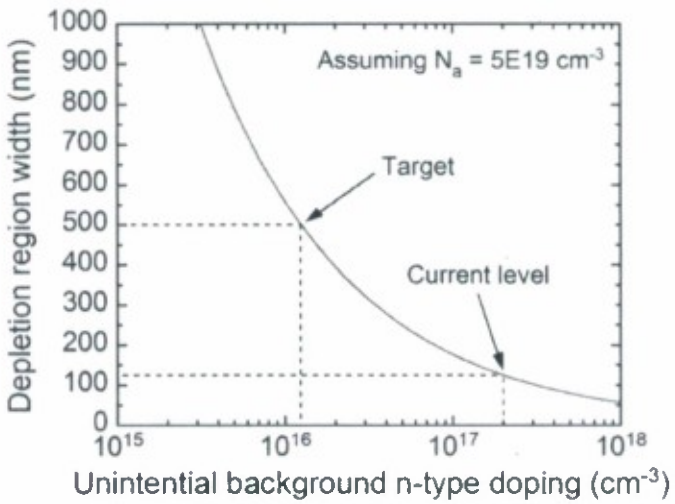

FIG. 12.9. Calculated dependence of depletion region width on unintentional background n-type doping in the active region of an InGaN-based solar cell.

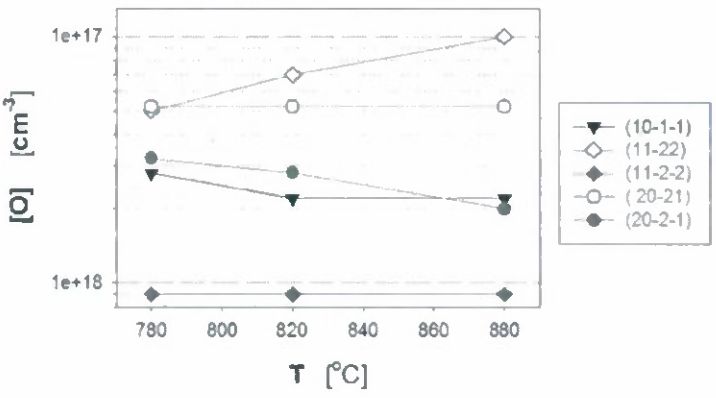

FIG. 12.10. Dependence of oxygen concentration on temperature for samples grown on GaN substrates with different crystallographic orientations. All samples were grown with a TEG flow of 35 sccm and an NH_3 flow of 4 slm, corresponding to a growth rate of about 0.12 nm/s.

13. Semipolar Solar Cells: Effects of QW Composition on Device Performance

Although the absorptance spectra of the semipolar solar cells discussed in Section 12 looked much sharper than for comparable *c*-plane devices, the FFs were still very low (ranging from 33.4 to 42.9%), similar to the FFs for *c*-plane solar cells with similar indium fractions in their QWs. As discussed above, a high unintentional background n-type doping in the active region could cause the depletion region width and hence the photocurrent to vary strongly with bias, potentially leading to the low FFs. Nevertheless, a strong correlation between QW composition and FF had been observed previously for Ga-polar *c*-plane solar cells, so a set of (20-21) solar cells with varying indium fraction in the QWs was also grown for comparison.

Figure 13.1(a) shows a cross-sectional schematic of the epitaxial structure of the set of $(20\bar{2}1)$ solar cells with varying indium fraction in the QWs. All structures had relatively wide barriers (~9 nm), similar to the barrier thicknesses used for the Ga-polar *c*-plane solar cells discussed in Section 11. Instead of changing the QW growth temperature as in Section 11, the indium fraction of the QWs was varied by changing the TMI flow in the QWs while holding the

(a)

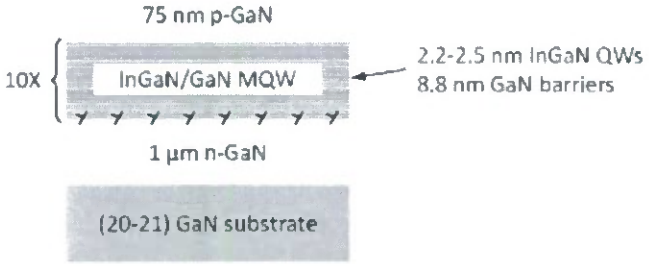

(b)

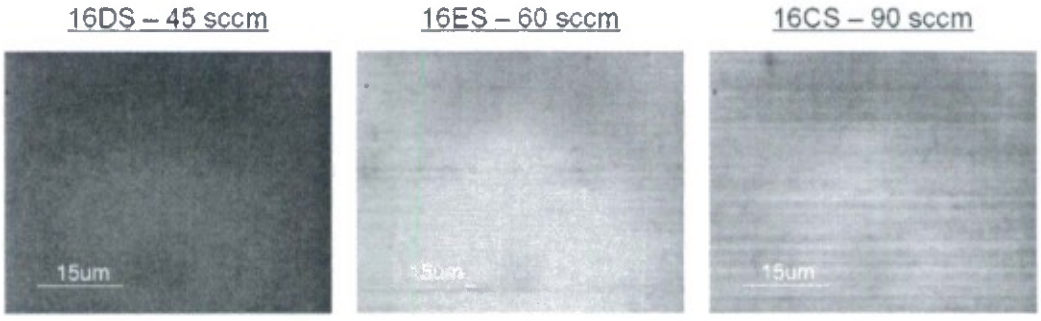

Fig. 13.1. (a) Cross-sectional schematic of the epitaxial structure of a set of (20-21) solar cells with a varying TMI flow in the QWs. (b) FLM images from the same set of devices.

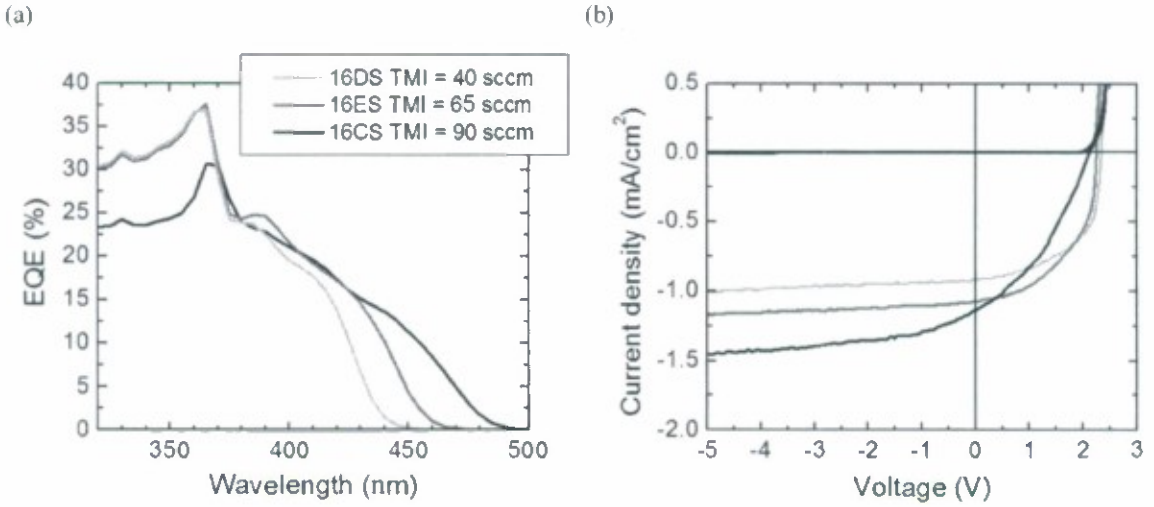

Fig. 13.2. (a) Dependence of EQE on wavelength for the set of (20-21) solar cells with varying TMI flow in QWs. (b) Dependence of dark and illuminated current density on voltage for the same set of devices.

TEG flow constant. Figure 13.1(b) shows FLM images for the samples with varying TMI flow (and hence indium fraction) in the QWs. The projection of the *c*-axis is towards the top of the page in these images. As expected, both the emission wavelength and MD density increased with increasing TMI flow, indicating that there was an increase in the indium fraction in the QWs, as confirmed by XRD measurements.

Figure 13.2(a) shows the dependence of EQE on wavelength for the same set of devices. As depicted in Fig. 13.2(a), the absorption edge increased with increasing TMI flow and indium fraction in the QWs. Figure 13.2(b) shows the dependence of dark and illuminated current

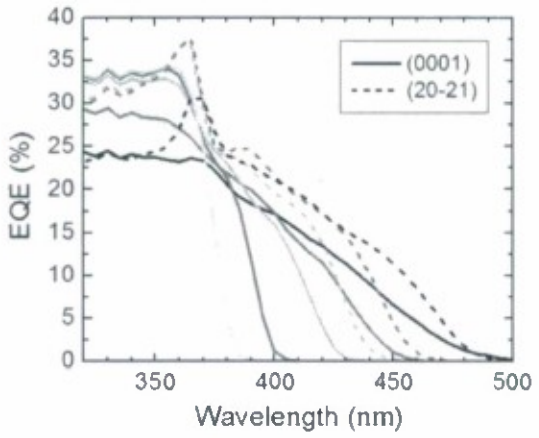

Fig. 13.3. Comparison of EQE spectra for (0001) and (20-21) 10X $In_xGa_{1-x}N$/GaN MQW solar cells with varying indium fraction, x, in the QWs.

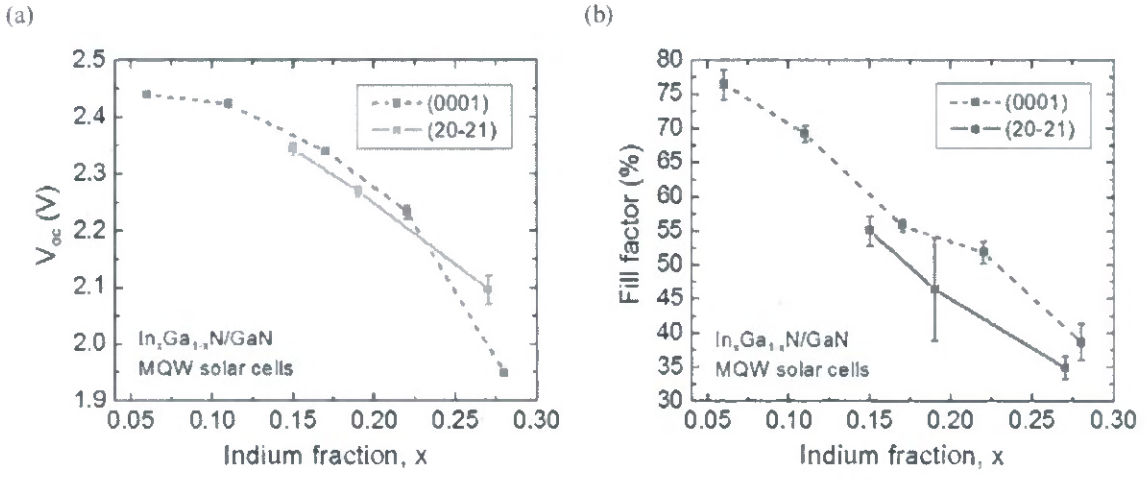

Fig. 13.4. (a) Dependence of V_{oc} on indium fraction for (0001) and (20-21) 10X $In_xGa_{1-x}N$/GaN MQW solar cells. (b) Dependence of FF on indium fraction for (0001) and (20-21) 10X $In_xGa_{1-x}N$/GaN MQW solar cells.

density on voltage for the same set of devices. As illustrated in Fig. 13.2(b), the shape of the *J-V* curves changed significantly with increasing TMI flow and indium fraction in the QWs, with an increase in the slope of the *J-V* curve around 0 V and a reduction in the sharpness of the knee of the *J-V* curve with increasing TMI flow and indium fraction in the QWs.

Qualitatively, the effects of indium fraction on semipolar device performance in Fig. 13.2 look very similar to the effects of indium fraction on device performance for the *c*-plane solar cells discussed in Section 11. To allow a direct comparison, EQE spectra are plotted on the same set of axes in Fig. 13.3 for both the 10X *c*-plane and 10X semipolar $In_xGa_{1-x}N$/GaN MQW solar cells with varying indium fraction in their QWs. For a given wavelength range, the semipolar samples exhibit a somewhat sharper absorption edge, as expected for QWs with smaller polarization-related electric fields. In this respect, the semipolar devices appear to have a slight advantage over similar *c*-plane devices. However, in terms of electrical properties such as V_{oc} and FF, the semipolar devices show little improvement over similar *c*-plane devices. Figures 13.4(a) and 13.4(b) show the dependence of V_{oc} and FF, respectively, on indium fraction in the QWs (estimated by XRD) for both the semipolar and *c*-plane devices. As expected, the V_{oc} decreased with increasing indium fraction and decreasing band gap and followed a similar trend for both sets of devices. However, the FF also decreased precipitously with increasing indium fraction for both sets of devices, with no visible improvement in FF for the semipolar devices. Thus, the data in Fig. 13.4(b) suggests that polarization is not the primary cause of the observed

degradation in FF with increasing indium fraction because the semipolar devices show similar FF trends even though the polarization-fields in the active regions of semipolar devices are much smaller than the polarization-fields in the active regions of *c*-plane devices. These results suggests that the degradation in FF with increasing content is related to some property associated with the indium content in QWs that is unrelated crystallographic orientation. One possibility is the effect of indium content on QW barrier height and thermionic emission out of the QWs, as discussed in more detail in the next section.

14. Semipolar Solar Cells: Effects of Barrier Thickness on Device Performance

Suspecting that device performance was limited by thermionic emission out of the QWs, we tried growing a series of devices with varying barrier thickness to see if tunneling would have a significant impact on carrier transport. Figure 14.1(a) shows a cross-sectional schematic of the epitaxial structure of the set of $(20\bar{2}1)$ solar cells with varying barrier thickness. All structures had 10 QWs with thicknesses of ~2.5 nm. Figure 14.1(b) shows FLM images for the samples with varying barrier thickness. The projection of the *c*-axis is towards the top of the page in these images. Neither the emission wavelength nor the MD density appeared to change

(a)

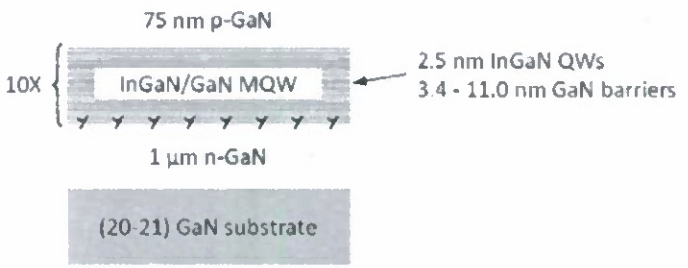

(b)

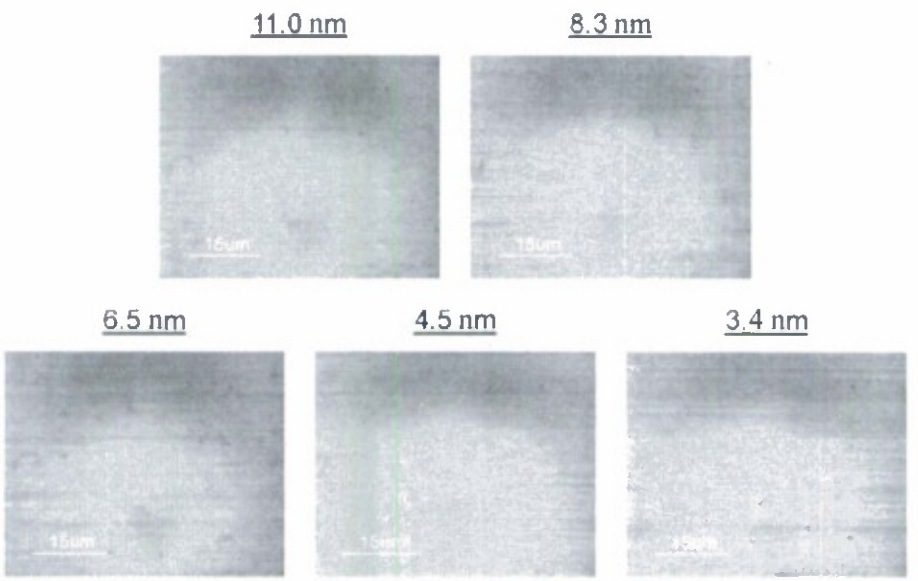

Fig. 14.1. (a) Cross-sectional schematic of the epitaxial structure of a set of (20-21) solar cells with varying barrier thickness. (b) FLM images from the same set of devices.

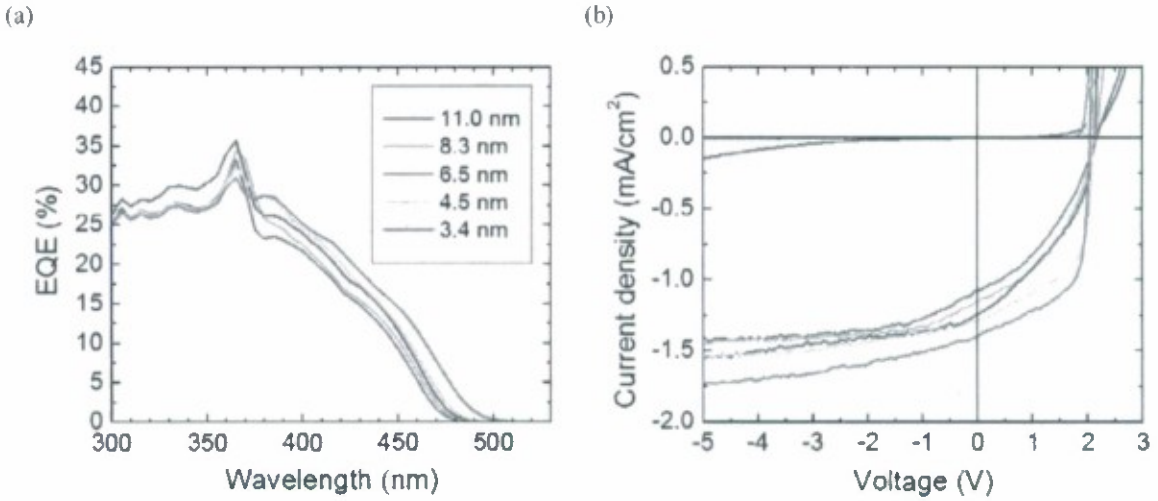

Fig. 14.2. Dependence of EQE on wavelength for the set of (20-21) solar cells with varying barrier thickness. (d) Dependence of dark and illuminated current density on voltage for the same set of devices.

significantly with increasing barrier thickness.

Figure 14.2(a) shows the dependence of EQE on wavelength for the same set of devices. As expected, the absorption edge became slightly longer with decreasing barrier thickness, as the magnitude of the built-in electric field that contributes to the total field in each QW should increase with decreasing barrier thickness for (20-21) QWs. Figure 14.2(b) shows the dependence of dark and illuminated current density on voltage for the same set of devices. As illustrated in Fig. 14.2(b), the shape of the *J-V* curves changed significantly with decreasing barrier thickness, with a decrease in the slope of the *J-V* curve around 0 V and a increase in the sharpness of the knee of the *J-V* curve with decreasing barrier thickness, as discussed in more detail below.

Figure 14.3(a) shows the dependence of J_{sc} on barrier thickness. As expected, the photocurrent at 0 V applied bias increased with decreasing barrier width due to an increase in tunneling current with decreasing barrier width. Likewise, as depicted in N8(b), the FF increased dramatically with barrier thickness, mostly due to an increase in the sharpness of the knee of the *J-V* curve with decreasing barrier thickness. Since the barriers for all of the devices are triangle-shaped and should become more triangular with decreasing (increasing) forward (reverse) bias, all of the devices should exhibit an increase in tunneling current with decreasing (increasing) forward (reverse) bias. However, the devices with wider barriers should exhibit a greater dependence of tunneling current with decreasing (increasing) forward (reverse) bias,

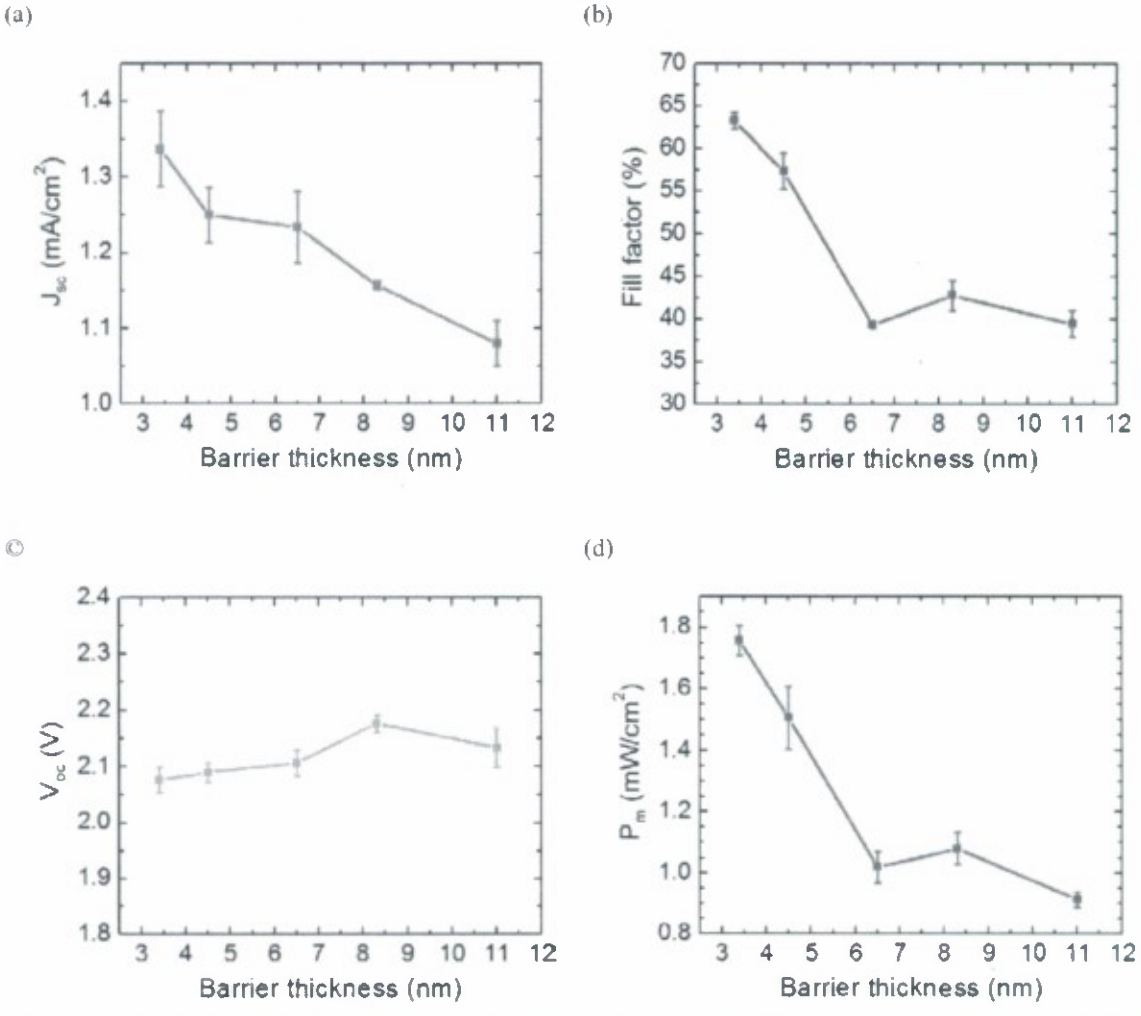

Fig. 14.3. (a) Dependence of J_{sc} on barrier thickness for the series of (20-21) solar cells with varying barrier thickness. (b) Dependence of FF on barrier thickness for the same set of devices. (c) Dependence of V_{oc} on barrier thickness for the same set of devices. (d) Dependence of P_m on barrier thickness for the same set of devices.

leading to lower FFs, as observed in Fig. 14.3(b). Figures 14.3(c) and 14.3(d) show the dependence of V_{oc} and P_m, respectively, on barrier thickness. As expected, the V_{oc} shows little dependence on barrier thickness, while P_m nearly doubles with decreasing barrier thickness, reflecting the trends in J_{sc} and FF presented in Figs. 14.3(a) and 14.3(b), respectively.

The above results suggest that it may be possible to create high-performance semipolar solar cells by growing devices with thin barriers. However, high-performance devices require more than 10 QWs, which increases the stress accumulated in the MQWs and can lead to the formation of unwanted misfit dislocations. Figure 14.4(a) shows a cross-sectional schematic of the epitaxial structure of a set of $(20\bar{2}1)$ MQW structures with varying barrier width and varying

(a)

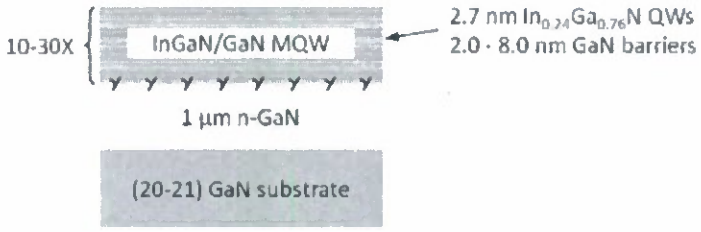

(b)

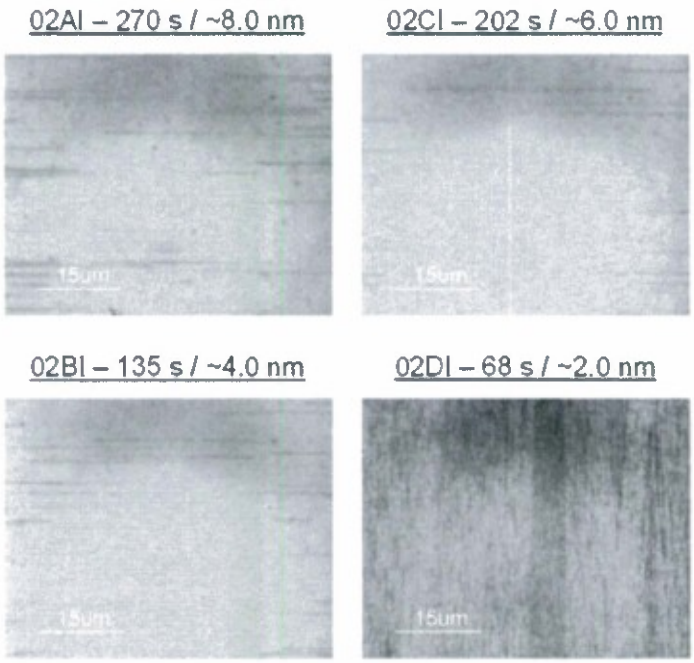

Fig. 14.4. (a) Cross-sectional schematic of the epitaxial structure of a set of (20-21) MQW structures with a varying number of QWs and varying barrier width. (b) FLM images of a set of 10X (20-21) InGaN/GaN MQW structures with 2.7 nm InGaN QWs and varying GaN barrier thickness.

number of QWs. All samples have 2.7 nm $In_{0.24}Ga_{0.76}N$ QWs and GaN barriers that vary in width from 2.0 to 8.0 nm. Figure 14.4(b) shows FLM images of a set of 10X (20-21) InGaN/GaN MQW structures with 2.7 nm InGaN QWs and varying GaN barrier thickness. The projection of the *c*-axis is towards the top of the page in these images. As shown in Fig. 14.4(b), the samples with 8.0, 6.0, and 4.0 GaN barriers exhibited a relatively low density of 1-D basal-plane MDs with a <11-20> line direction, much like all of the previous samples discussed above. However, the sample with 2.0 nm GaN barriers exhibited non-basal-plane MDs in addition to the basal-plane MDs. Moreover, the emission wavelength was dramatically redshifted compared to

the three other samples, exhibiting emission in the green region of the spectrum for identical growth conditions.

Figure 14.5 shows FLM images of a set of 20X (20-21) InGaN/GaN MQW structures with 2.7 nm InGaN QWs and varying GaN barrier thickness. The projection of the *c*-axis is towards the top of the page in these images. As shown in Fig. 14.5, the sample with 8.0 GaN barriers exhibited a relatively low density of 1-D basal-plane MDs with a <11-20> line direction. With decreasing barrier thickness, though, the samples exhibited an increasing density of non-basal-plane MDs.

Figure 14.6 shows FLM images of a set of 30X (20-21) InGaN/GaN MQW structures with 2.7 nm InGaN QWs and varying GaN barrier thickness. The projection of the *c*-axis is towards the top of the page in these images. As shown in Fig. 14.6, the sample with 8.0 GaN barriers exhibited a relatively low density of 1-D basal-plane MDs with a <11-20> line direction. Much like the 20X MQW samples in Fig. 14.5, though, these samples also exhibited an increasing density of non-basal-plane MDs with decreasing barrier thickness. Finally, Fig. 14.7 shows a set of AFM images from the same set of 30X (20-21) InGaN/GaN MQW structures with

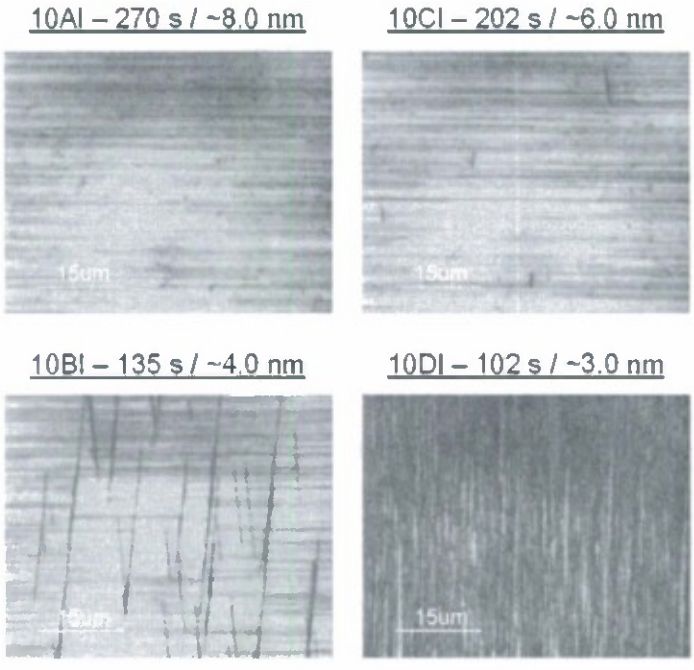

Fig. 14.5. FLM images of a set of 20X (20-21) InGaN/GaN MQW structures with 2.7 nm InGaN QWs and varying GaN barrier thickness.

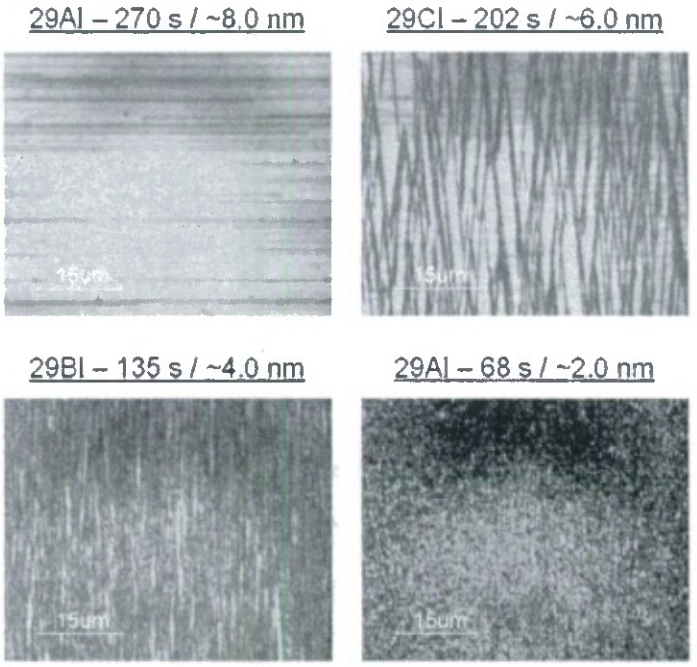

Fig. 14.6. FLM images of a set of 30X (20-21) InGaN/GaN MQW structures with 2.7 nm InGaN QWs and varying GaN barrier thickness.

2.7 nm InGaN QWs and varying GaN barrier thickness. The projection of the *c*-axis is towards the top right of the page in these images. The effect of the non-basal-plane MDs on the surface morphology is clearly visible in this image, with lines that run along the projection of the c-axis corresponding roughly to the density of lines in the non-basal-plane MDs in the FLM images in Fig. 14.7. Also, as expected, the RMS roughness increased significantly with decreasing barrier width and increasing non-basal-plane MD density.

To determine the effect of non-basal-plane MD density on device performance, a set of devices was grown with 3 nm barriers and with the number of QWs varied from 10 to 40. As expected, the devices with more than 20 periods exhibited a high density of non-basal-plane MDs and a high degree of diode leakage under both forward and reverse bias (data not shown), resulting in poor device performance. These experiments suggest that semipolar planes are not suitable for the growth of solar cells with MQWs with thin barriers due to the formation of non-basal-plane MDs. These non-basal-plane MDs form due to the nonzero resolved stresses on the multiple glide planes present for semipolar orientations. In contrast, the *c*-plane growth orientation has a no resolved stresses on the glide-dominant basal plane and it has relatively low oxygen incorporation, thus avoiding both of the

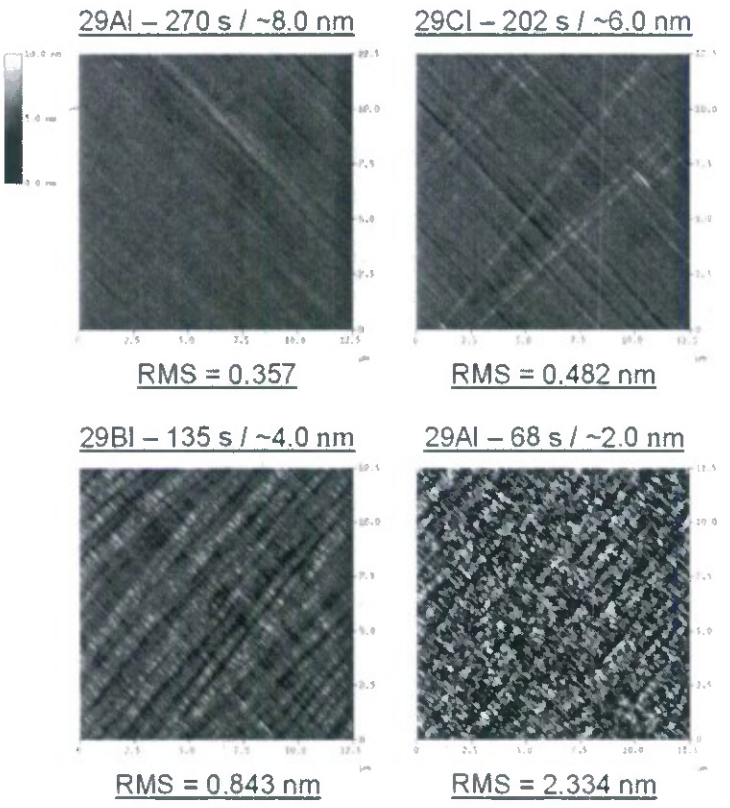

Fig. 14.7. AFM images of a set of 30X (20-21) InGaN/GaN MQW structures with 2.7 nm InGaN QWs and varying GaN barrier thickness.

major problems associated with growth on semipolar planes. In addition, as shown in Fig. 13.4, *c*-plane devices perform the same, if not better, than semipolar devices with similar barrier thicknesses and QW compositions. Thus, it is our conclusion that the most promising path forward is to try to grow Ga-polar *c*-plane InGaN solar cells with thin barriers and a high number of periods. Although this approach should be limited by the formation of v-defects for devices with thin barriers grown on sapphire (see Section 5), this problem can be circumvented by growing devices on Ga-polar *c*-plane free-standing substrates with a low density of threading dislocations.